


## LEIA discovery of the longest-lasting and most energetic stellar X-ray flare ever detected

XUAN MAO <sup>1,2</sup> HE-YANG LIU <sup>1</sup> SONG WANG <sup>1,3</sup> ZHIXING LING,<sup>1,2,3</sup> WEIMIN YUAN,<sup>1,2</sup> HUAQING CHENG,<sup>1</sup> HAIWU PAN,<sup>1</sup> DONGYUE LI,<sup>1</sup> FABIO FAVATA,<sup>4,5</sup> TUO JI,<sup>6</sup> JUJIA ZHANG,<sup>7,8,9</sup> XINLIN ZHAO,<sup>1,2</sup> JING WANG,<sup>1,10,11</sup> ZHIMING CAI,<sup>12</sup> ALBERTO J. CASTRO-TIRADO,<sup>13,14</sup> YANFENG DAI,<sup>1</sup> LICAI DENG,<sup>1,2,15</sup> XU DING,<sup>7,16,17</sup> KAIFAN JI,<sup>2,7,16,17</sup> CHICHUAN JIN,<sup>1,2,3</sup> YAJUAN LEI,<sup>1</sup> HUALI LI,<sup>1</sup> JUN LIN,<sup>2,7,17,18</sup> HUAQIU LIU,<sup>12</sup> MINGJUN LIU,<sup>1,2</sup> SHUAI LIU <sup>1</sup> YUAN LIU,<sup>1</sup> HUI SUN,<sup>1</sup> SHENGLI SUN,<sup>19</sup> XIAOJIN SUN,<sup>19</sup> JIANRONG SHI,<sup>1,2</sup> JIANGUO WANG <sup>7,16</sup> JINGXIU WANG,<sup>1,2</sup> WENXIN WANG,<sup>1</sup> JIANYAN WEI,<sup>1,2</sup> LIPING XIN,<sup>1</sup> DINGRONG XIONG,<sup>7</sup> CHEN ZHANG,<sup>1,2</sup> WENDA ZHANG,<sup>1</sup> YONGHE ZHANG,<sup>12</sup> XIAOFENG ZHANG,<sup>12</sup> DONGHUA ZHAO,<sup>1</sup> AND GUIPING ZHOU<sup>1,2</sup>

<sup>1</sup>National Astronomical Observatories, Chinese Academy of Sciences, Beijing 100101, China

<sup>2</sup>School of Astronomy and Space Science, University of Chinese Academy of Sciences, Chinese Academy of Sciences, Beijing 100049, China

<sup>3</sup>Institute for Frontiers in Astronomy and Astrophysics, Beijing Normal University, Beijing 102206, China

<sup>4</sup>INAF - Osservatorio Astronomico di Palermo, Piazza del Parlamento, 1, 90134 Palermo, Italy

<sup>5</sup>Department of Physics, Imperial College London, Exhibition Road, London SW7 2AZ, United Kingdom

<sup>6</sup>Polar Research Institute of China, Shanghai 200136, China

<sup>7</sup>Yunnan Observatories, Chinese Academy of Sciences, Kunming 650216, China

<sup>8</sup>International Centre of Supernovae, Yunnan Key Laboratory, Kunming 650216, China

<sup>9</sup>Key Laboratory for the Structure and Evolution of Celestial Objects, Chinese Academy of Sciences, Kunming, 650216, China

<sup>10</sup>Guangxi Key Laboratory for Relativistic Astrophysics, School of Physical Science and Technology, Guangxi University, Nanning 530004, China

<sup>11</sup>GXU-NAOC Center for Astrophysics and Space Sciences, Nanning, 530004, China

<sup>12</sup>Innovation Academy for Microsatellites, Chinese Academy of Sciences, Shanghai 201210, China

<sup>13</sup>Instituto de Astrofísica de Andalucía (IAA-CSIC), Granada, Spain

<sup>14</sup>Unidad Asociada al CSIC, Departamento de Ingeniería de Sistemas y Automática, Escuela de Ingenierías, Universidad de Málaga, Málaga, Spain

<sup>15</sup>Department of Astronomy, China West Normal University, Nanchong 637002, China

<sup>16</sup>Key Laboratory for the Structure and Evolution of Celestial Objects, Chinese Academy of Sciences, Kunming 650216, China

<sup>17</sup>Center for Astronomical Mega-Science, Chinese Academy of Sciences, Beijing 100012, China

<sup>18</sup>Yunnan Key Laboratory of Solar Physics and Space Science, Kunming 650216, China

<sup>19</sup>Shanghai Institute of Technical Physics, Chinese Academy of Sciences, Shanghai, 200083, China

### ABSTRACT

*LEIA* (Lobster Eye Imager for Astronomy) detected a new X-ray transient on November 7, 2022, identified as a superflare event occurring on a nearby RS CVn-type binary HD 251108. The flux increase was also detected in follow-up observations at X-ray, UV and optical wavelengths. The flare lasted for about 40 days in soft X-ray observations, reaching a peak luminosity of  $\sim 1.1 \times 10^{34}$  erg s<sup>-1</sup> in 0.5–4.0 keV, which is roughly 60 times the quiescent luminosity. Optical brightening was observed for only one night. The X-ray light curve is well described by a double “FRED” (fast rise and exponential decay) model, attributed to the cooling process of a loop arcade structure formed subsequent to the initial large loop with a half-length of  $\sim 1.9$  times the radius of the host star. Time-resolved X-ray spectra were fitted with a two-temperature *apec* model, showing significant evolution of plasma temperature, emission measure, and metal abundance over time. The estimated energy released in the *LEIA* band is  $\sim 3 \times 10^{39}$  erg, suggesting this is likely the most energetic X-ray stellar flare with the longest duration detected to date.

Corresponding author: He-Yang Liu, Song Wang, Zhixing Ling, Weimin Yuan

liuheyang@nao.cas.cn, songw@bao.ac.cn, lingzhixing@bao.ac.cn, wmy@nao.cas.cn

*Keywords:* X-ray transient sources (1852); Stellar flares (1603); Stellar activity (1580); RS Canum Venaticorum variable stars (1416)

## 1. INTRODUCTION

Solar and stellar flares are sudden and intense electromagnetic radiation enhancement detectable across a wide range of frequencies typically lasting from minutes to hours. These flares are believed to be caused by the rapid release of magnetic energy during the impulsive reconnection of twisted magnetic fields in the outer atmosphere (e.g., Shibata & Magara 2011; Walkowicz et al. 2011). Although stellar flares are believed to be generated by similar processes as solar flares (see also Lin & Forbes 2000), the diverse characteristics of stellar species and their space environments can lead to a wider range of flare parameters, including peak luminosity, duration, and total energy release. In particular, some stellar flares, known as superflares, can release over ten to a million times the energy of the largest solar flares ( $\sim 10^{32}$  erg; Emslie et al. 2012) and have been observed in various stars (e.g., Maehara et al. 2012; Shibayama et al. 2013; Candelaresi et al. 2014; Hawley et al. 2014; Davenport 2016; Notsu et al. 2019; Okamoto et al. 2021). Such superflares with extremely powerful bursts of energy released by stars, can help give insight into both the nature of stellar activities and the potential challenges faced by planets in close proximity to them.

RS Canum Venaticorum (RS CVn) type binaries are composed of two late-type stars, typically with one being a giant or subgiant and the other a dwarf or subgiant. The binary system is notable for their intense stellar activities, including highly energetic and prolonged flares (Pandey & Singh 2012; Martínez et al. 2022) and large star spots due to magnetic interactions between the stars (Drake 2006; Drake et al. 2014). Violent flares lasting up to several days with released energies of  $\sim 10^{38}$  erg has been reported on RS CVn-type Star GT Mus (Sasaki et al. 2021). Moreover, the system generally have synchronized rotational and orbital periods due to strong tidal forces (Karmakar et al. 2023). The synchronization will enhance magnetic interactions and can lead to heightened stellar activity. These characteristics make RS CVn binaries valuable for studying stellar magnetism and dynamics in binary system.

HD 251108 is a nearby RS CVn-type star located at R.A.=06:04:15.0, Dec=12:45:51, with a distance of  $504.7_{-4.6}^{+4.8}$  pc (Gaia EDR3 measurement; Bailer-Jones et al. 2021). The primary star is a K2 type giant with an effective temperature of  $T_{\text{eff}} = 4545_{-138}^{+405}$  K and a surface gravity of  $\log g = 2.13_{-0.09}^{+0.17}$  [cgs] (Anders et al. 2019), however, details about its companion star remain

unclear. HD 251108 is also identified as the X-ray source 2RXS J060415.1+124554, which is detected by *ROSAT* with a flux of  $8.246 \times 10^{-12}$  erg s $^{-1}$  cm $^{-2}$  in 0.1–2.4 keV (Boller et al. 2016), and by *eROSITA* with a flux of  $7.518 \times 10^{-12}$  erg s $^{-1}$  cm $^{-2}$  in 0.2–2.3 keV (Predehl et al. 2021; Merloni et al. 2024). The corresponding quiescent X-ray luminosity is  $\sim 10^{32}$  erg s $^{-1}$ .

*LEIA* (Lobster Eye Imager for Astronomy, Zhang et al. 2022; Ling et al. 2023) is an operative wide-field X-ray monitor (see Section 2.1 for a brief introduction). On November 7, 2022, a burst event was first detected by *LEIA* as a new X-ray transient, which was later identified as a superflare occurring on the star HD 251108. Following this detection, a multi-wavelength campaign was conducted on this source, including observations and monitoring by *Swift*, *NICER*, ASAS-SN, GWAC, BOOTES, and Lijiang 2.4-meter telescope (see Table 1). These observations revealed that the flare from HD 251108 was extraordinarily luminous and prolonged. And the estimated energy release and duration suggests it may be the most energetic and longest-lasting X-ray stellar flare ever recorded.

In this work, we present our study on the exceptional stellar flare that occurred on HD 251108. The paper is organized as follows. First, we describe the observation and data reduction of this source in X-ray, UV and optical bands in Section 2. Next, we present a detailed analysis on time-resolved spectra and light curves in Section 3. Then the physical scenarios of the flare cooling process and the stellar activity are discussed in Section 4, followed by a summary in Section 5.

## 2. OBSERVATIONS AND DATA REDUCTION

On November 7, 2022, *LEIA* detected a new X-ray transient, designated LXT 221107A (Ling et al. 2022). Within the approximate 3-arcminute error circle of this transient, there exists a known *ROSAT* source, 2RXS J060415.1+124554, associated with the RS CVn binary HD 251108. However, the flux of this known *ROSAT* source is ten times lower than that of LXT 221107A. An optical counterpart coincided with HD 251108 was identified by GWAC on November 7, 2022. To explore the nature of LXT 221107A, we performed a *Swift* target of opportunity observation on November 9, 2022. *Swift*-XRT detected an X-ray source spatially consistent with HD 251108, and no additional candidates were found in the LXT 221107A localization error region. The XRT spectrum was well-fitted by a collisionally ionized

plasma model, giving a flux still significantly higher than the quiescent level of HD 251108. These observational evidences confirm that LXT 221107A was a superflare event on HD 251108. To study this exceptional flare in greater detail, further observations and monitoring over the following three months were conducted, as described in subsequent sections.

### 2.1. *LEIA*

*LEIA* is a focusing X-ray telescope with a large spontaneous field-of-view (FoV) of about 340 square degrees and a soft X-ray energy bandpass of 0.5–4.0 keV, enabled by novel lobster eye micro-pore optics technology (Ling et al. 2023). As a pathfinder of the Einstein Probe (*EP*) mission (Yuan et al. 2022), *LEIA* was launched on July 27, 2022 into a Sun-synchronous orbit with a height of 550 km on board the SATech-01 satellite of the Chinese Academy of Sciences (CAS). It has been operational since achieving its first light in August 2022 (Zhang et al. 2022). *LEIA* has a spatial resolution of  $\sim 5$  arcmin (full width at half maximum, FWHM) and a sensitivity of  $2\text{--}3 \times 10^{-11}$  erg s $^{-1}$  cm $^{-2}$  with a 1000 s exposure.

*LEIA* detected LXT 221107A on November 7, 2022, and subsequently conducted a series of 40 observations to monitor the source from November 7 to November 18. During this period, *LEIA* found that the flux of LXT 221107A increased continuously, reaching its peak on November 8, 2022, before beginning a gradual decline.

The *LEIA* data was reduced using the data reduction software developed for the Einstein Probe (*EP*) mission (Liu et al., in preparation), and the calibration database (CALDB) generated from both on-ground and in-orbit calibration campaigns (Cheng et al., in preparation; Cheng et al. 2024).

### 2.2. *Swift/XRT*

A *Swift* target of opportunity observation (Target ID: 15410, PI: D.Y. Li) was conducted following the detection of LXT 221107A by *LEIA*. The XRT onboard *Swift* began observations on November 9, 2022, and detected the source (Li et al. 2022), noting that the flux was already lower than the peak level detected by *LEIA*. Over the following two months, we conducted four additional observations using the *Swift*. The data of these five observations were downloaded from HEASARC, and were calibrated and screened through the standard reduction procedures using the `HEASOFT` package (v6.32.1) and *Swift*/XRT CALDB (version 20230725).

### 2.3. *NICER*

The first *NICER* observation of LXT 221107A began on November 9, 2022 (Pasham et al. 2022), and the observed flux was consistent with *Swift*/XRT’s measurements (see Figure 1). *NICER* continued to observe the source for nearly three months, with observation IDs ranging from 5203530101 to 5203530169, totaling an exposure time of 170 ks. These observations revealed that this event was an extremely long-lasting flare and detected another weaker flare about 40 days after LXT 221107A.

Data from all 69 *NICER* observations were obtained from the HEASARC website, except for observation ID 5203530129, which had an exposure time of 0 seconds. The data were processed using the `HEASOFT` package (v6.32.1), incorporating `NICERDAS` (version 10) and *NICER*/XTI CALDB (version 20221001).

### 2.4. *Swift/UVOT*

Along with XRT, the UVOT onboard *Swift* also conducted observations of LXT 221107A. For each of five *Swift* observations, four UVOT filters—U, uvw1, uvw2, and uvm2—were used to capture the images, except during the second observation. Aperture photometry was performed using the `uvotsource` task with *Swift*/UVOTA CALDB (version 20240201). The U and uvm2 data from the first observation were excluded because the source was located in bad area of the image.

### 2.5. *ASAS-SN*

We searched the ASAS-SN Sky Patrol v1.0 and examined the light curve of HD 251108, which was generated using Aperture Photometry. A brightening was observed in three consecutive observations in *g* band at the night of November 7, 2022, confirming that LXT 221107A was a high-level stellar flare occurring on HD 251108.

The bottom panel of the Figure 1 shows all ASAS-SN *g* band observations of HD 251108 during the flare period. The brightening was found only on the detection day of LXT 221107A, indicating that its optical flux returned to quiescent levels within three days. This return to quiescence is considerably quicker than that in the soft X-ray band. Such differing timing behaviors across wavelengths are common in solar and stellar flares (Benz 2002; Benz & Güdel 2010).

### 2.6. *GWAC*

During the X-ray flare, an optical brightening of about 0.6 magnitude relative to its quiescent level was also detected by the Ground-based Wide Angle Cameras (GWAC; Wang et al. 2021; Xin et al. 2024) in its routine

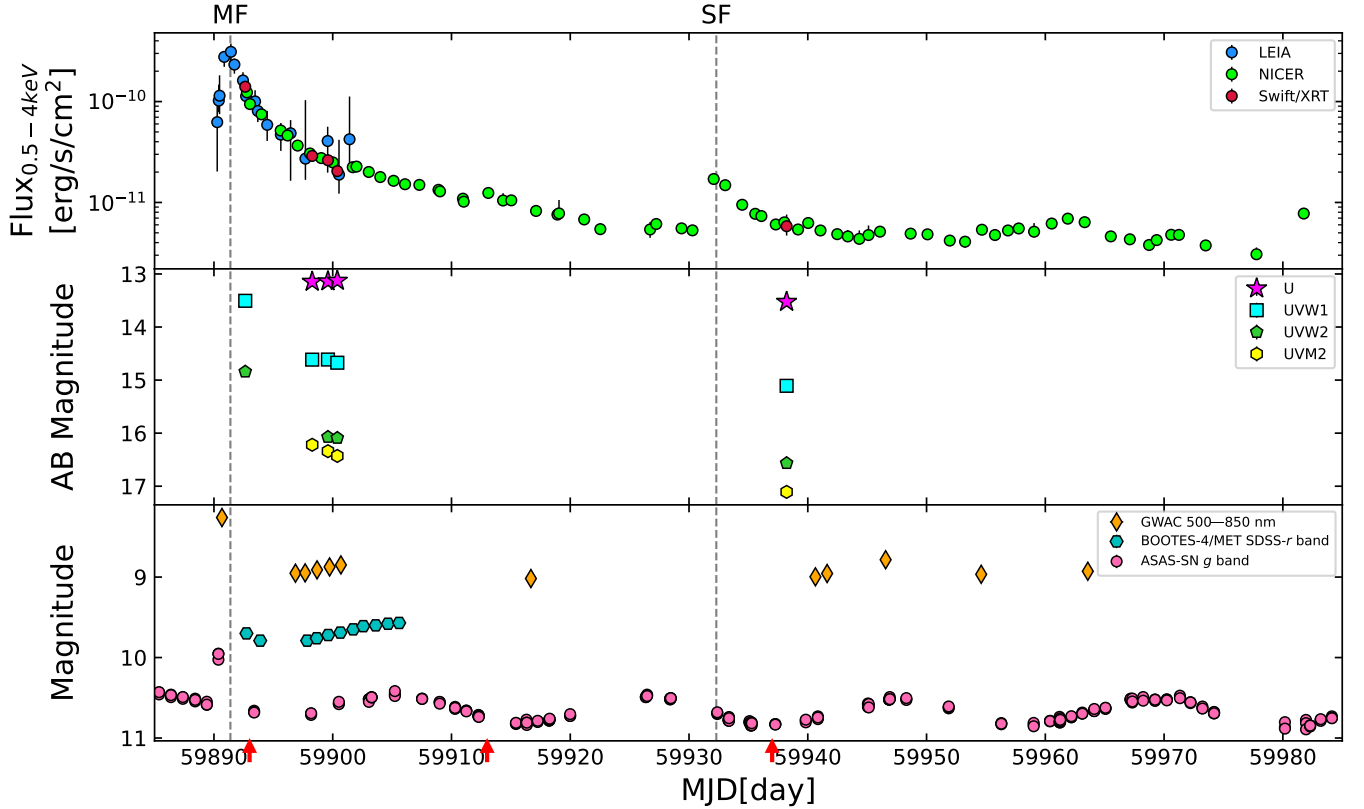


**Figure 1.** The comprehensive light curve of HD 251108 in soft X-ray (top panel), UVOT bands (middle panel), and ground-based optical photometry (bottom panel). For the soft X-ray (top panel), the unabsorbed flux in the 0.5–4.0 keV for each spectrum was estimated using the `cflux` model during spectral fitting in `xspec` (see Section 3.1 for more details on the spectral fitting process). The grey dashed lines mark the peak times of the main flare (MF) and the secondary flare (SF). The red arrows at the bottom indicate when the three optical spectra were taken (see Section 2.8).

**Table 1.** Multi-wavelength observations on HD 251108

Instrument	Obs-Date	Waveband
<i>LEIA</i>	from 2022-11-07 to 2022-11-18	Soft X-ray
<i>Swift</i>	from 2022-11-09 to 2022-12-25	Soft X-ray/UV
<i>NICER</i>	from 2022-11-09 to 2023-02-06	Soft X-ray
ASAS-SN	from 2022-11-02 to 2023-02-09	optical
GWAC	from 2022-11-07 to 2023-01-19	optical
BOOTES-4/MET	from 2022-11-09 to 2022-11-22	optical
Lijiang 2.4m Telescope	2022-11-10, 2022-11-30 and 2022-12-24	optical

survey. As one of main ground facilities of the Space-based multi-band Variable Objects Monitor (SVOM; Wei et al. 2016), GWAC monitored about 2000 square degrees of the sky in a cadence of 15 seconds. The observation was carried out in white filter, which was calibrated into *R* band of Johnson-Bessel system. The general behavior of GWAC light curve was consistent with the observations of ASAS-SN. Each data point in Figure

1 represents the mean magnitude of the observations at that night.

### 2.7. *BOOTES-4/MET*

Follow-up optical observations were conducted using the *BOOTES-4/MET* 0.6m optical telescope from November 9 to November 22 (Xiong et al. 2022). After applying flat field and bias corrections, aperture pho-

tometry was performed using PyRAF<sup>1</sup>. Two comparison stars, TYC 725-825-1 and TYC 725-489-1, were selected, and the SDSS DR16 catalog (Lyke et al. 2020) was used as the reference. The light curves in all three bands ( $g$ ,  $r$  and  $i$ ) are consistent with those observed by ASAS-SN and GWAC. However, the brightening phase was not detected due to the delayed start of the observations.

### 2.8. Lijiang 2.4-meter Telescope

Using the Lijiang 2.4m telescope, three high-resolution spectra of HD 251108 were obtained on November 10, November 30 and December 24, 2022, respectively. The resolution is  $\sim 32,000$  at 550 nm (Wang et al. 2019). The observed spectra were reduced using the IRAF software (Tody 1986, 1993) following standard procedures, and then corrected to vacuum wavelength.

As shown in Figure 2, the strong H $\alpha$  emission line in all three spectra confirms the active nature of HD 251108. Notably, the spectrum obtained on November 10, two days after the X-ray flare peak, shows a significant enhancement in the Balmer lines (e.g., H $\alpha$ , H $\beta$ , H $\gamma$ , and H $\delta$ ). This enhancement suggests the energy transport from corona to the chromosphere during the flare.

## 3. ANALYSIS AND RESULTS

### 3.1. X-ray Spectral Fitting

Given the significantly longer exposure and higher photon counts compared to the observations of *LEIA* and *Swift*/XRT, we began with the *NICER* spectral fitting. A one-temperature thin thermal plasma model (TBabs\*apec; Smith et al. 2001) was first adopted. However, most of the spectra cannot be well fitted; for instance, 14 out of the first 20 spectral fittings had a reduced  $\chi^2$  higher than 2 (i.e.,  $\chi^2_{\nu} > 2$ ). We then incorporated a second apec model, setting the metallicity ( $Z$ ) of both cool and hot plasma components to be the same, and fixed the redshifts to zero. After initial fittings, we found the hydrogen column density ( $N_{\text{H}}$ ) and the temperature of the cool component ( $kT_{\text{cool}}$ ) were consistent across observations, allowing us to fix them at their mean values:  $(6.3 \pm 1.1) \times 10^{20} \text{ cm}^{-2}$  and  $1.2 \pm 0.1 \text{ keV}$ , respectively. The constancy of  $N_{\text{H}}$  suggests no mass ejections along the line of sight, while  $kT_{\text{cool}}$  may represent the quiescent-state corona temperature. This two-temperature (TBabs\*(apec+apec); 2T apec) model effectively fitted most spectra, and a three-temperature (TBabs\*(apec+apec+apec); 3T apec) model did not

significantly improve the fits<sup>2</sup>. The best-fit parameters for each *NICER* observation are listed in Table A.1.

Similar to the *NICER* spectral analysis, the spectra from *LEIA* and *Swift*/XRT were also fitted using the 2T apec model. The  $N_{\text{H}}$  and  $kT_{\text{cool}}$  were fixed to those *NICER*-derived values. The metallicity ( $Z$ ) is fixed to be  $0.07 Z_{\odot}$ , the average metallicity value derived from the spectral fittings of the first nine *NICER* observations.

In Figure 3, the hot component's emission measure ( $EM_{\text{hot}}$ ) shows a notable rise and fall consistent with the light curve, reaching a peak two orders of magnitude higher than that in quiescence. And the hot component's temperature ( $kT_{\text{hot}}$ ) varied by a factor of around 3. In contrast, the cool component's temperature ( $kT_{\text{cool}}$ ) remains stable, but its emission measure ( $EM_{\text{cool}}$ ) decreases in line with the light curve, which is also reported by Osten et al. (2010). The initial *NICER* observations also reveal a slight decrease in metallicity ( $Z$ ). Similar variations in metallicity during stellar flares have been reported by Pandey & Singh (2012) and Karmakar et al. (2023).

### 3.2. X-ray Light Curve

Following common practice (Sasaki et al. 2021; Pandey & Singh 2012), the X-ray light curve was generated using photon flux corrected for absorption in 0.5–4.0 keV. Initially, the light curve is fitted using the widely adopted Fast (linear) Rise and Exponential Decay (FRED) model (Osten et al. 2016; Günther et al. 2020; Sasaki et al. 2021). The model is expressed as

$$c(t) = \begin{cases} c_{\text{q}} & , (t < t_{\text{ST}}); \\ (c_{\text{p}} - c_{\text{q}}) \times \frac{t - t_{\text{ST}}}{t_{\text{p}} - t_{\text{ST}}} + c_{\text{q}} & , (t_{\text{ST}} \leq t < t_{\text{p}}); \\ (c_{\text{p}} - c_{\text{q}}) \times \exp\left(-\frac{t - t_{\text{p}}}{\tau_d}\right) + c_{\text{q}} & , (t_{\text{p}} \leq t). \end{cases}$$

Here  $t$ ,  $c(t)$ ,  $t_{\text{ST}}$ ,  $t_{\text{p}}$ ,  $c_{\text{p}}$ , and  $c_{\text{q}}$  are time, photon flux, the time when the photon flux starts to increase, the time when the photon flux reaches the peak, the corresponding peak photon flux, and the photon flux when the star is in X-ray quiescence, respectively.  $\tau_d$  is the e-folding time during the decay phase of the flares, and  $\tau_r = t_{\text{p}} - t_{\text{ST}}$  is the rise time. The time of the first *LEIA* observation is set to be 0. The  $c_{\text{q}}$  was fixed to the mean value of photon flux after flare (i.e.  $2.6 \times 10^{-3} \text{ counts cm}^{-2}$  for MJD>59940), and the remaining four parameters ( $t_{\text{ST}}$ ,  $t_{\text{p}}$ ,  $c_{\text{p}}$ , and  $\tau_d$ ) were derived from model fitting.

<sup>2</sup> For only a few spectra, the 3T apec model provided a better fitting. However, to maintain consistency in our analysis, we adopted the 2T apec model for all spectra fittings. The derived X-ray flux from spectral fitting remains consistent between the two models.

<sup>1</sup> <https://iraf-community.github.io/pyraf.html>. PyRAF is a command language for IRAF based on the Python scripting language that can be used in place of the existing IRAF CL.

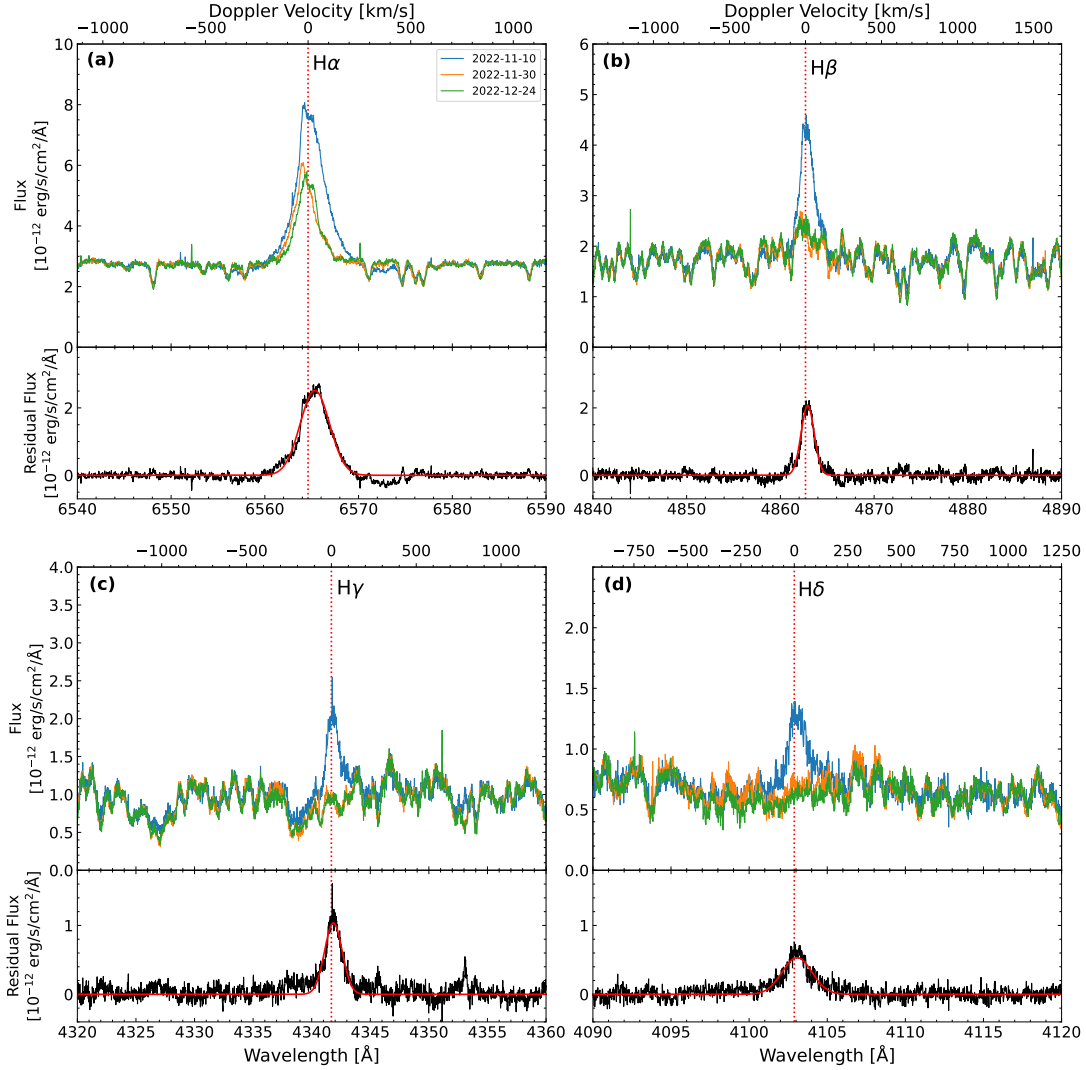


**Figure 2.** The Balmer-regions of optical spectra of HD 251108 taken by the Lijiang 2.4 m telescope. In plot (a)-(d), the residual spectra are presented in the bottom panels, each fitted by a Gaussian function (red solid line).

The initial fitting results show that a single FRED model cannot adequately describe the light curve during the decay phase of the main flare. The decay deviates from a pure exponential shape, with a faster decay in the early phase (MF1) and a slower decay in the late phase (MF2, as shown by the grey dotted line in the top panel of Figure 3). To address this, an additional FRED model was introduced for MF2, and significantly improved the fit (depicted by the red solid line in Figure 3). The light curve of SF can be well fitted with a single FRED model. The best-fit parameters are showed in Table 2.

### 3.3. Flare Parameters

The flare durations are defined as  $\tau_{\text{MF}} = \tau_{\text{r,MF1}} + \tau_{\text{d,MF1}} + \tau_{\text{d,MF2}} = 1090$  ks ( $\sim 12.6$  days) for MF, and

$\tau_{\text{SF}} = \tau_{\text{r,SF}} + \tau_{\text{d,SF}} = 382$  ks ( $\sim 4.4$  days) for SF. The total energy released by the MF in the 0.5–4.0 keV band is estimated to  $E_{\text{X,MF}} = E_{\text{X,MF1}} + E_{\text{X,MF2}} = 3 \times 10^{39}$  erg, which is  $10^7$  times the energy of the largest solar flares. Figure 4 shows the flare duration versus peak luminosity and flare energy, comparing these quantities with several RS CVn-type flares from previous studies (Tsuru et al. 1989; Endl et al. 1997; Franciosini et al. 2001; Pandey & Singh 2012; Tsuboi et al. 2016; Sasaki et al. 2021), with X-ray luminosities and energies converted uniformly to the 0.5–4.0 keV range using `webpimms` with a multi-temperature `apec` model. Additionally, we included superflares from pre-main-sequence (PMS) stars studied by Getman & Feigelson (2021), along with flares of cool stars derived from XMM-Newton data (Pye et al. 2015), although their luminosities and energies are plotted in the 0.5–8.0 keV and 0.2–12 keV bands, respectively. It is

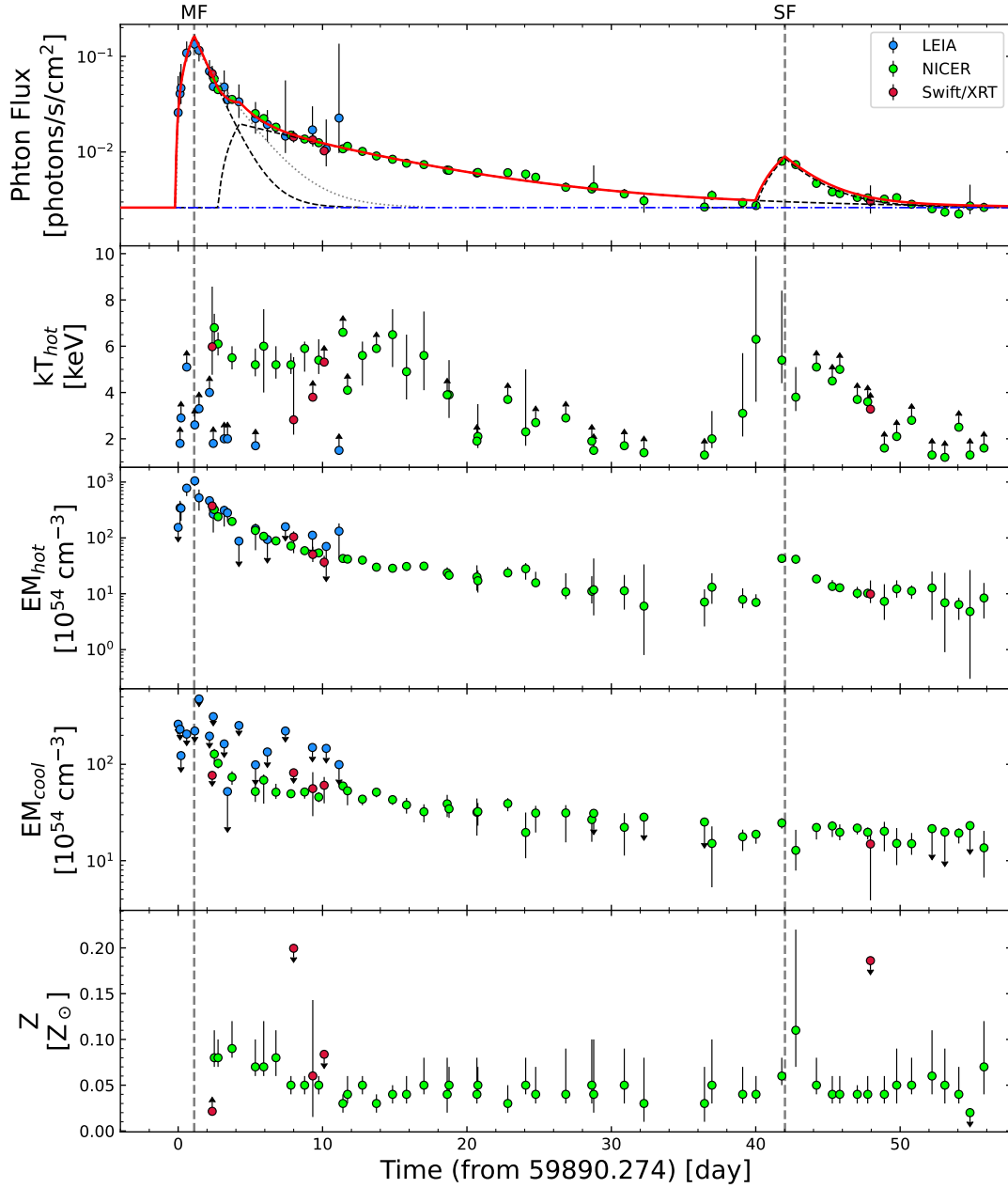


**Figure 3.** X-ray light curve and evolution of spectral parameters from *LEIA*, *NICER* and *Swift/XRT* spectra. From top to bottom, it displays: the X-ray photon flux light curve in the 0.5–4.0 keV, the time variations in the temperature of the hot plasma component, the emission measures of both the cool and hot plasma components, and the metal abundance. The grey dashed lines are consistent with those in Figure 1. In the top panel, each black dashed line represents an FRED model employed to fit the light curve. The blue dot-dashed line indicates the quiescent photon flux, while the red solid line shows the combined fitting result. The grey dotted line illustrates the single FRED fitting of the main flare (MF), which does not adequately describe the decay phase.

**Table 2.** Best-fit Parameters of the X-ray light curve

	$t_p^a$ (days since MJD=59890.274)	$c_p^b$ (counts s <sup>-1</sup> cm <sup>-2</sup> )	$\tau_r^c$ (ks)	$\tau_d^d$ (ks)	$L_{X,p}^e$ (10 <sup>32</sup> erg s <sup>-1</sup> )	$f_X^f$ (10 <sup>-5</sup> erg cm <sup>-2</sup> )	$E_X^g$ (10 <sup>38</sup> erg)
MF1	1.1±0.3	0.16±0.04	112±50	109±9	110.8±29.7	6.0±1.9	18.3±5.7
MF2	4.2±0.2	0.020±0.001	128±12	869±34	13.3±1.7	4.1±1.1	12.4±1.7
SF	42.0±0.2	0.009±0.001	177±18	205±24	5.8±0.8	0.6±0.1	1.7±0.3

<sup>a</sup>The flare peak time since the observation start time of the first detection by *LEIA*.

<sup>b</sup>The peak photon flux in the 0.5–4.0 keV band.

<sup>c</sup>Flare rise time, which is the difference between the flare start time and its peak time (namely,  $t_p - t_{ST}$ ).

<sup>d</sup>Flare e-folding decay time.

<sup>e</sup>The flare peak luminosity in 0.5–4.0 keV with absorption corrected, calculated by  $L_{X,p} = 4\pi d^2 F_{X,p}$ , where  $d$  is the distance of HD 251108 and  $F_{X,p}$  is the flare peak flux, assumed to be isotropic.

<sup>f</sup>Time-integrated X-ray fluence in 0.5–4.0 keV of the flare calculated by  $f_X = F_{X,p}(\tau_r/2 + \tau_d)$ .

<sup>g</sup>The total energy released during the flare, i.e.,  $E_X = L_{X,p}(\tau_r/2 + \tau_d) = 4\pi d^2 f_X$ .

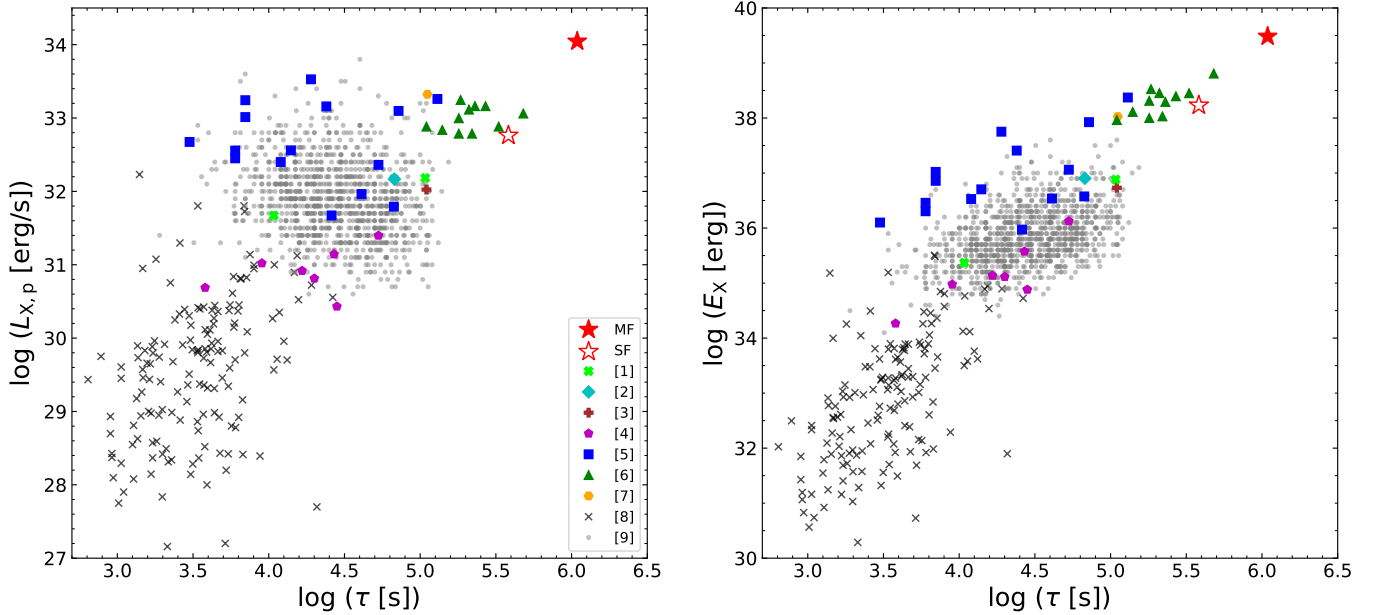


**Figure 4.** Flare duration ( $\tau$ ) versus flare peak luminosity ( $L_{X,p}$ , left panel) and flare energy ( $E_X$ , right panel) for MF and SF, along with stellar flares reported by [1]: Tsuru et al. (1989), [2]: Endl et al. (1997), [3]: Franciosini et al. (2001), [4]: Pandey & Singh (2012), [5]: Tsuboi et al. (2016), [6]: Sasaki et al. (2021), [7]: Karmakar et al. (2023), [8]: Pye et al. (2015), [9]: Getman & Feigelson (2021). The flares from [1]–[7] all took place in RS CVn-type binary systems, with the energy band converted into 0.5–4.0 keV. The energy bands are 0.2–12 keV in [8] and 0.5–8.0 keV in [9], respectively.



clear from Figure 4 that the MF of HD 251108 is located in the most upper right corner of both panels, making it the brightest, longest-lasting, and most energetic flare among all those compared, potentially representing the largest X-ray stellar flare ever detected. Notably, the parameters of the SF also rank among the highest in this context.

In addition, these stellar flares reported above as well as solar flares and microflares reported by Feldman et al. (1995) and Shimizu (1995) are plotted in the  $\log T$ - $\log EM$  diagram (Figure 5), partitioned by isolines of flaring loop length and magnetic field strength. These isolines are derived using Equations (5) and (6) in Shibata & Yokoyama (1999). The maximum  $T_{\text{hot}} \approx 79$  MK (i.e.,  $kT_{\text{hot}} = 6.8$  keV), derived from *NICER* data, serves as the lower limit for the plasma peak temperature of the main flare due to lack of constraints from *LEIA* observations. The diagram shows that the MF of HD 251108 has magnetic field strength and plasma temperature comparable to other RS CVn-type stellar flares while displaying one of the longest flaring loop lengths and the largest emission measure.

In previous studies, no additional non-thermal components have been detected in the high-energy band from stellar flares (Favata & Schmitt 1999; Osten et al. 2016). Thus, we can estimate the energy released across the entire X-ray range (0.1–200 keV) using the best-fitting 2T *apec* model in 3.1. Although the spectra evolve, the conversion factor from flux in the 0.5–4 keV range to the 0.1–200 keV range, derived from *NICER* spectra during the early decay phase of the main flare, is approximately 1.9. Therefore, the total energy released during the MF across the X-ray range is approximately  $\sim 5.7 \times 10^{39}$  erg.

### 3.4. Optical Spectra

Using the three optical spectra obtained by Lijiang 2.4m telescope, we analyzed the emission line properties during the flares. To obtain the residual spectrum, we subtracted the average of the later two quiescent spectra from the first (flare) spectrum. The residual profiles of four Balmer lines were fitted with single-Gaussian model (see bottom panels of Figure 2, plots (a)-(d)). The derived parameters are presented in Table A.4. The maximum projected velocity  $V_{\text{max}}$ , was calculated based on the minimum and maximum wavelengths where the residual profile exceeds  $1\sigma$  above the continuum. The high  $V_{\text{max}}$  values suggest fast-moving chromospheric plasma, possibly driven by energy injections from flare-accelerated electrons.

## 4. DISCUSSION

### 4.1. Cooling Process and Flare Loop Geometry

As mentioned in Section 3.2, the X-ray light curve of the MF shows a double-exponential decay. Such a decay is commonly seen in many stellar flares (Reale et al. 2004; Getman et al. 2008; Wargelin et al. 2008), which is believed to be similar to some large solar flares (Lin & Forbes 2000; Aschwanden & Alexander 2001; Lin 2002; Kashapova et al. 2021). The flare process can be typically explained as follows (Reale et al. 2004). Initially, magnetic reconnection in an active region on the stellar surface triggers a heat pulse, igniting a large magnetic loop and causing the initial flare burst. Once the first heat pulse subsides, the flare quickly fades, but residual heat ignites a secondary system of loops, akin to an arcade of loops observed in solar flares. The cooling of these loops leads to the slower decay observed later. The constant  $T_{\text{hot}}$  before and around the time of the secondary peak ( $t_{\text{p, MF2}}$ ) supports the idea that the event is due to the cooling of an established loop system, rather than a brand-new loop causing a subsequent, weaker flare. A similar conclusion was discussed in Reale et al. (2004). In this scenario, the flare duration, temperature, and emission measure obtained in Section 3 can be used to infer the geometry of the magnetic loops and the physical properties of the flaring plasma.

The detailed calculations and results for the loop parameters are presented in Appendix B. The magnetic field strength and flaring loop length derived from the cooling timescale of MF align with those indicated by the *EM*-*T* diagram in Figure 5. The estimated loop length is approximately  $1.8 \times 10^{12}$  cm (about 1.9 times the stellar radius, see Appendix C).

A comparison with eight flares from RS CVn-type stars reported by Pandey & Singh (2012) shows that the estimated loop length  $L$  in our work is at least an order of magnitude larger. According to the RTV scaling law, where  $p \propto L^{-1}T^3$  (see Appendix B), this results in a much smaller pressure and, consequently, a weaker magnetic field. The longevity of such an extensive loop structure may primarily be due to the star's low gravitational acceleration. The estimated magnetic field strength and half-length of flaring loop are consistent with the Figure 5 as well.

It is important to note that the loop size may be greatly underestimated, as the actual peak temperature  $kT_{\text{hot, peak}}$  could significantly exceed 6.8 keV. For instance, assuming  $kT_{\text{hot, peak}} = 10$  keV yields a loop length of approximately  $2.2 \times 10^{12}$  cm, while  $kT_{\text{hot, peak}} = 20$  keV results in a length of  $\sim 3.2 \times 10^{12}$  cm (see Table B.1). Additionally, the choice of energy band can influence the shape of the light curve, affecting the derived cooling timescales and loop parameters. We there-

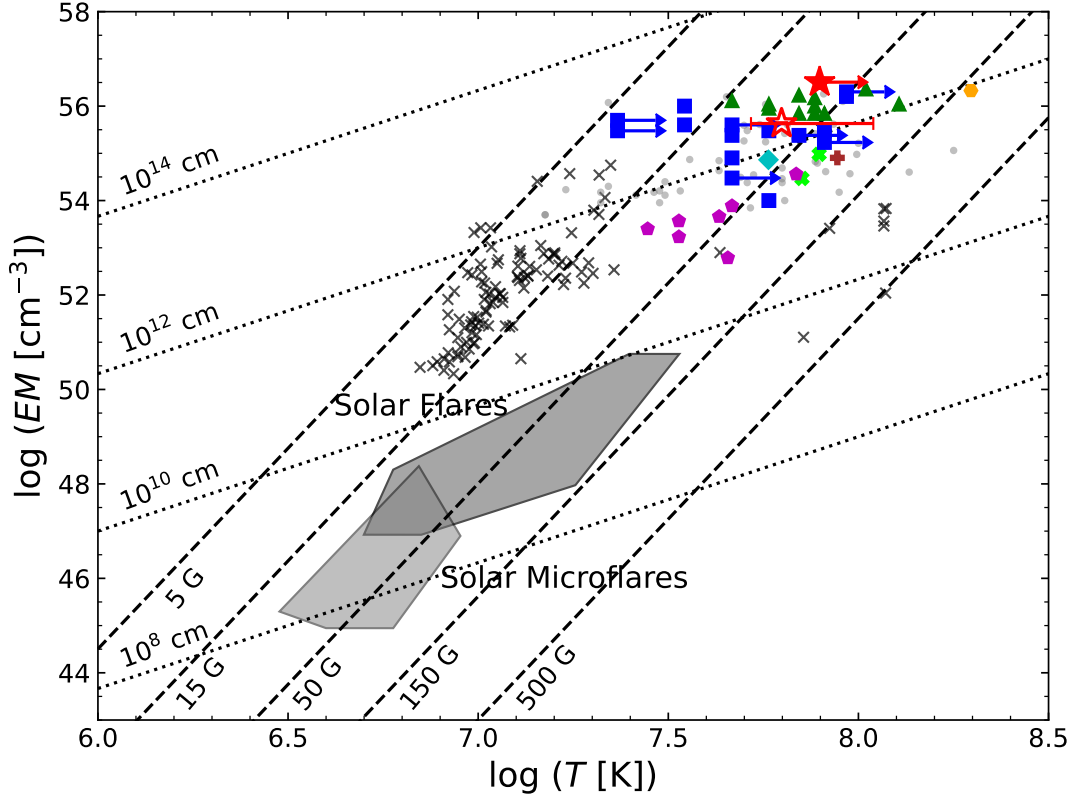


**Figure 5.** Emission measure ( $EM$ ) versus plasma temperature ( $T$ ). The symbols are the same as those in Figure 4, with the exception that the grey points are from Getman et al. (2021), which represent 55 bright superflares selected from Getman & Feigelson (2021). Plus filled polygons symbolized solar flares (Feldman et al. 1995) and solar microflares (Shimizu 1995). The dashed lines indicate the  $EM$ - $T$  relation ( $EM \propto B^{-5}T^{17/2}$ ) for a constant magnetic field, and the dotted lines show the  $EM$ - $T$  relation ( $EM \propto L^{5/3}T^{8/3}$ ) constrained by certain loop lengths (Shibata & Yokoyama 1999).

fore attempted to fit the light curve in the 0.1–200 keV range (based on the best-fitting spectral models), again assuming  $kT_{\text{hot,peak}} = 10$ –20 keV. The results suggest that the loop length could increase by 10% to 30%. Note that several other factors, such as sustained heating (Reale et al. 1997), may also influence the estimation of the loop length. A more comprehensive analysis of the flaring processes is required, but such an analysis is beyond the scope of this work and will be addressed in future research.

#### 4.2. Stellar activity and stellar parameters

As shown in Figure C2, besides ellipsoidal modulation, the light curves exhibit clear variability caused by cool spots or warm faculae, indicating a stellar cycle longer than 10 years, which is commonly observed in RS CVn-type stars (Martínez et al. 2022). The flare occurred when the amplitude of the modulation increased to a high value, suggesting an expansion of star spot area and hence a higher stellar activity. A long-term joint fitting, with the unspotted brightness treated as a free but shared parameter over each year, can help break the

degeneracy between the spots and the unspotted brightness of the star (Zhao et al. 2024). Figure C3 shows the best-fit models to the light curves and the sizes and configurations of the two spots (i.e., a large polar spot and a small equatorial spot). Along with the largeness of the flaring loop, the occurrence in the polar magnetic active region supports the hypothesis that MF was only slightly affected by the stellar rotation. The detailed fitting results are provided in Appendix C. Notably, the large separation of the binary ( $\approx 50 R_{\odot}$ ) indicates that the magnetic loops were unlikely to extend to the companion star.

We examined the magnetic activity of HD 251108 by introducing the X-ray luminosity to bolometric luminosity ratio,  $R_X = L_X/L_{\text{bol}}$  (Pallavicini et al. 1981). Using the bolometric luminosity estimated from the derived stellar parameters (see Appendix C) and the quiescent X-ray luminosity detected by *NICER*, we derived  $R_X \sim 5 \times 10^{-4}$ , placing HD 251108 within the saturated region ( $R_X \sim 10^{-3}$ ), indicative of high X-ray activity (Wright et al. 2011).

The stellar parameters of HD 251108 is estimated using the long-term light curves obtained from ASAS-SN (see Appendix C for details). The mass of the primary giant was estimated to be  $M_{\text{giant}} = 0.26_{-0.01}^{+0.04} M_{\odot}$ , and the companion is suggested to be a G/K-type main sequence star, with  $T_{\text{eff,com}} = 5400_{-68}^{+31}$  K and a mass of  $M_{\text{com}} = 0.79_{-0.14}^{+0.14} M_{\odot}$ . The rotation period is determined to be around 40 days and the Roche lobe filling factor is  $\approx 90\%$ . The small mass and large Roche lobe filling factor suggest that the giant has undergone significant mass transfer to the companion. And we note that this mass estimate for the primary is in good agreement with the orbital period-white dwarf mass relation (Rappaport et al. 1995).

## 5. SUMMARY

We reported a superflare event, happened on the RS CVn-type star HD 251108, detected by *LEIA* and followed by multi-wavelength observations. The detected X-ray flux rise lasted for nearly 40 days with peak X-ray luminosity estimated to be  $\sim 1.1 \times 10^{34}$  erg s $^{-1}$  in 0.5–4.0 keV, making it the longest-lasting and potentially the most luminous stellar X-ray flare. A change of e-folding timescale was found during the flare decay phase, thus a double-FRED model was chosen to fit the X-ray light curve. The fit result indicated that the main energy release occurred in the fast decay phase. The time resolved X-ray spectra were well fitted with the *apec* model with two temperature components. The derived flare parameters ( $T_{\text{hot}}$ ,  $EM_{\text{hot}}$ , duration and peak luminosity) are all located at the upper end of the parameter spaces constructed by superflares reported in previous studies. The flaring loop length is roughly estimated to be  $\sim 1.9R_{\text{giant}}$  around the peak of the flare, and the magnetic field strength  $B$  is about 50 G. The derived energy release in 0.5–4.0 keV is  $\sim 3 \times 10^{39}$  erg, which suggests this is possibly the most-energetic-ever-detected X-ray stellar flare.

Such an energetic flare is actually not unexpected since the magnetic activity of HD 251108 is rather high ( $R_{\text{X}} \approx 5 \times 10^{-4}$ ). In addition, an activity cycle longer than a decade is evident in the ASAS-SN photometric data. The flare occurred during an epoch when the amplitude of the light curve variation significantly increased, indicating an expansion of the star spot area and hence enhanced stellar activity. This is consistent with the large polar star spots derived from the light curve modeling. Apart from the intense magnetic activities that foster conditions for the superflare, the low surface gravity of HD 251108 also contributes to the prolonged duration of this flare. The light curve fitting also

suggest the unseen companion is possibly a G-/K-type main sequence star with a mass nearly three times that of the giant, indicating significant mass transfer has occurred between these two stars.

With the launch of *EP* on 9 January 2024, which monitors the X-ray sky with much larger field-of-view and wider range of timescales than *LEIA*, it is expected to detect a massive amount of stellar flares, which can fundamentally deepen our understanding of this explosive phenomenon.

This work is based on the data obtained with *LEIA*, a pathfinder of the Einstein Probe mission, which is supported by the Strategic Priority Program on Space Science of Chinese Academy of Sciences (grant Nos. XDA15310000, XDA15052100). We acknowledge the support by the National Key Research and Development Programs of China (NKRDPC) under grant Nos. 2022YFF0711404, 2021YFA0718500, 2022SKA0130102, 2022SKA0130100, 2019YFA0405504 and 2019YFA0405000, National Natural Science Foundation of China (NSFC) under grant Nos. 12103061, 11988101, 12273057, 12203071, 11833002, 12090042, 12103047, 12473016, and the Strategic Priority Program on Space Science of Chinese Academy of Sciences (grant Nos. XDB41000000, XDB0550200). AJCT acknowledges support from the Spanish Ministry projects PID2020-118491GB-I00 and PID2023-151905OB-I00 and Junta de Andalucía grant P20\_010168 and from the Severo Ochoa grant CEX2021-001131-S funded by MCIN/AEI/ 10.13039/501100011033. This work also made use of data supplied by NASA through the NICER team and Swift team, and software provided by the High Energy Astrophysics Science Archive Research Center (HEASARC), which is a service of the Astrophysics Science Division at NASA/GSFC. We acknowledge use of the VizieR catalog access tool, operated at CDS, Strasbourg, France, and of Astropy, a community-developed core Python package for Astronomy (Astropy Collaboration, 2013). This research made use of Photutils (Bradley et al. 2020), an Astropy package for detection and photometry of astronomical sources.

*Facilities:* Einstein Probe (Yuan et al. 2022), NICER, Swift, SVOM/GWAC, BOOTES-4/MET, Lijiang:2.4m

*Software:* Python, Astropy, Heasoft (Arnaud 1996), IRAF

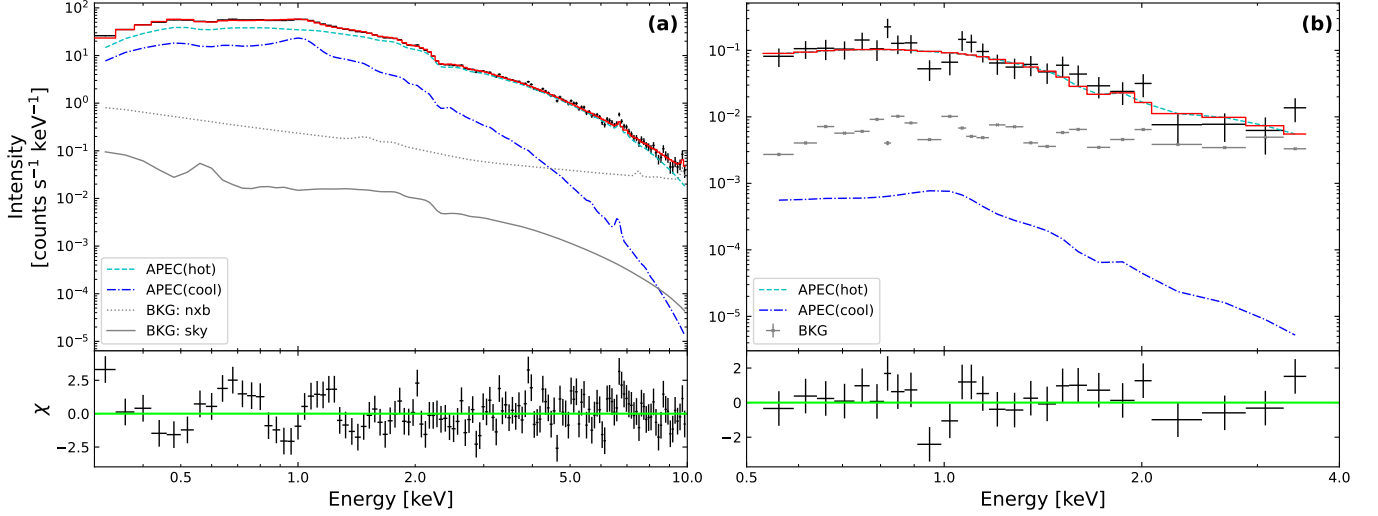


**Figure A1.** Two examples of X-ray spectra during MF, fitted by  $\text{TBabs}^*(\text{apec}+\text{apec})$  model (red solid line) composed of a hot (cyan dashed) and a cool (blue dashdot) plasma component. (a) The *NICER* spectra is corresponding to the No.01 observation in Table A.1, and (b) the *LEIA* spectra is corresponding to the No.05 observation in Table A.2.

## APPENDIX

### A. BEST-FIT SPECTRAL PARAMETERS

All best-fit parameters of X-ray and optical spectra discussed in Section 3.1-3.4 were listed in this section. In addition, spectral fitting for *LEIA* and *NICER* are illustrated in Figure A1.

**Table A.1.** Best-fit Spectral parameters for each *NICER* observation

No.	Obs. Start time (UTC)	Exposure time (s)	$kT_{\text{hot}}^a$ (keV)	$EM_{\text{hot}}^b$ ( $10^{54} \text{ cm}^{-3}$ )	$EM_{\text{cool}}^b$ ( $10^{54} \text{ cm}^{-3}$ )	$Z^c$ ( $Z_{\odot}$ )	$L_X$ ( $10^{32} \text{ erg s}^{-1}$ )	$\chi^2_{\nu}$ (d.o.f.) <sup>d</sup>
01	2022-11-09 18:39:51	2185	$6.8^{+0.6}_{-0.7}$	$321.4^{+14.2}_{-11.2}$	$127.7^{+16.8}_{-22.0}$	$0.08^{+0.03}_{-0.01}$	$37.6 \pm 0.8$	1.55 (121)
02	2022-11-10 00:52:32	7195	$6.1 \pm 0.5$	$239.6^{+8.5}_{-6.6}$	$102.4^{+8.3}_{-11.8}$	$0.08^{+0.02}_{-0.01}$	$28.8 \pm 0.6$	1.40 (127)
03	2022-11-11 00:06:50	2035	$5.5 \pm 0.5$	$196.9^{+9.0}_{-8.2}$	$73.5^{+11.3}_{-12.2}$	$0.09^{+0.03}_{-0.01}$	$22.8 \pm 0.5$	1.45 (112)
04	2022-11-12 14:49:50	1774	$5.2^{+0.7}_{-0.5}$	$135.9^{+8.4}_{-4.4}$	$52.2 \pm 11.5$	$0.07^{+0.03}_{-0.01}$	$15.7^{+0.7}_{-0.4}$	1.28 (106)
05	2022-11-13 04:46:49	1153	$6.0^{+1.6}_{-2.0}$	$106.8^{+19.4}_{-6.4}$	$68.6^{+9.8}_{-29.5}$	$0.07^{+0.05}_{-0.01}$	$14.1 \pm 0.4$	0.99 (104)
06	2022-11-14 01:06:21	1221	$5.2^{+0.8}_{-0.6}$	$88.3^{+6.0}_{-7.9}$	$51.4^{+11.4}_{-7.6}$	$0.08^{+0.03}_{-0.02}$	$11.2^{+0.4}_{-0.3}$	1.40 (101)
07	2022-11-15 02:02:58	5715	$5.2^{+0.5}_{-0.4}$	$71.6^{+3.5}_{-3.6}$	$49.5^{+4.9}_{-4.6}$	$0.05 \pm 0.01$	$9.3 \pm 0.2$	1.56 (115)
08	2022-11-16 00:48:34	9399	$5.9^{+0.3}_{-1.0}$	$59.0^{+4.9}_{-1.9}$	$51.6^{+2.5}_{-7.6}$	$0.05 \pm 0.01$	$8.4 \pm 0.2$	1.45 (121)
09	2022-11-17 00:14:34	9916	$5.4^{+0.9}_{-0.6}$	$53.9^{+3.6}_{-2.6}$	$45.7^{+5.7}_{-5.2}$	$0.05 \pm 0.01$	$7.6 \pm 0.2$	1.51 (122)
10	2022-11-18 16:26:50	2017	$> 6.6$	$42.8^{+2.6}_{-1.9}$	$59.6^{+3.6}_{-6.6}$	$0.03 \pm 0.01$	$6.8^{+0.3}_{-0.2}$	1.19 (104)
11	2022-11-19 00:05:01	3628	$> 4.1$	$41.7^{+8.4}_{-2.0}$	$53.1^{+4.6}_{-15.5}$	$0.04^{+0.02}_{-0.01}$	$6.9^{+0.2}_{-0.4}$	1.05 (108)
12	2022-11-20 00:50:41	6480	$5.6^{+0.6}_{-1.3}$	$40.0^{+3.7}_{-1.9}$	$43.5^{+2.9}_{-5.9}$	$0.05 \pm 0.01$	$6.1 \pm 0.2$	1.34 (114)
13	2022-11-21 00:08:13	4981	$> 5.9$	$29.9^{+2.8}_{-1.1}$	$51.4^{+2.2}_{-5.9}$	$0.03 \pm 0.01$	$5.4 \pm 0.2$	1.08 (108)
14	2022-11-22 02:56:48	3270	$6.5^{+1.1}_{-1.4}$	$28.6^{+3.2}_{-2.0}$	$43.0^{+3.4}_{-5.1}$	$0.04 \pm 0.01$	$5 \pm 0.2$	1.30 (103)

Table A.1 continued

Table A.1 (continued)

No.	Obs. Start time (UTC)	Exposure time (s)	$kT_{\text{hot}}^a$ (keV)	$EM_{\text{hot}}^b$ ( $10^{54} \text{ cm}^{-3}$ )	$EM_{\text{cool}}^b$ ( $10^{54} \text{ cm}^{-3}$ )	$Z^c$ ( $Z_{\odot}$ )	$L_X$ ( $10^{32} \text{ erg s}^{-1}$ )	$\chi^2_{\nu}$ (d.o.f.) <sup>d</sup>
15	2022-11-23 02:08:27	1394	$4.9^{+1.6}_{-1.2}$	$30.8^{+5.6}_{-4.9}$	$37.9^{+6.9}_{-7.1}$	$0.04^{+0.02}_{-0.01}$	$4.6^{+0.1}_{-0.2}$	1.36 (94)
16	2022-11-24 07:03:26	2105	$5.6^{+1.9}_{-1.5}$	$31.2^{+4.1}_{-3.5}$	$32.2^{+6.3}_{-7.2}$	$0.05^{+0.03}_{-0.01}$	$4.5 \pm 0.2$	0.96 (100)
17	2022-11-25 21:44:08	563	>3.9	$23.6^{+6.1}_{-4.1}$	$38.9^{+9.3}_{-10.5}$	$0.04^{+0.04}_{-0.02}$	$4.1^{+0.3}_{-0.2}$	1.46 (86)
18	2022-11-26 00:50:10	3686	$3.9^{+1.5}_{-1.0}$	$21.4^{+5.4}_{-3.4}$	$34.5^{+4.8}_{-6.7}$	$0.05^{+0.02}_{-0.01}$	$3.9^{+0.3}_{-0.2}$	1.41 (110)
19	2022-11-27 23:09:36	814	>1.9	$20.0^{+12.3}_{-8.7}$	$31.8^{+12.4}_{-13.6}$	$0.04^{+0.04}_{-0.01}$	$3.3^{+0.3}_{-0.2}$	1.01 (97)
20	2022-11-28 00:43:16	4893	$2.1^{+1.4}_{-0.5}$	$17.1^{+9.1}_{-6.6}$	$32.3^{+7.4}_{-9.2}$	$0.05^{+0.02}_{-0.01}$	$3.1 \pm 0.1$	1.86 (127)
21	2022-11-30 02:26:37	1074	>3.7	$23.6^{+6.7}_{-3.0}$	$39.1^{+5.5}_{-6.5}$	$0.03^{+0.02}_{-0.01}$	$3.8^{+0.3}_{-0.2}$	1.01 (93)
22	2022-12-01 08:12:47	3667	$2.3^{+2.7}_{-0.6}$	$28.0^{+7.4}_{-10.1}$	$19.6^{+12.0}_{-9.0}$	$0.05^{+0.03}_{-0.01}$	$3.2^{+0.6}_{-0.2}$	1.28 (100)
23	2022-12-02 00:49:37	1390	>2.7	$15.7^{+9.0}_{-2.3}$	$31.2^{+5.9}_{-11.6}$	$0.04^{+0.03}_{-0.01}$	$3.2^{+0.3}_{-0.2}$	1.47 (96)
24	2022-12-04 02:51:36	557	>2.9	$10.8^{+12.5}_{-2.8}$	$31.3^{+6.4}_{-15.8}$	$0.04^{+0.05}_{-0.01}$	$2.5 \pm 0.2$	1.35 (83)
25	2022-12-05 22:05:45	1065	>1.9	$11.1^{+9.5}_{-4.4}$	$26.7^{+7.0}_{-11.0}$	$0.05^{+0.05}_{-0.02}$	$2.3^{+0.2}_{-0.1}$	1.02 (97)
26	2022-12-06 01:16:10	487	>1.5	$11.8^{+31.0}_{-7.7}$	<38.3	$0.04^{+0.06}_{-0.02}$	$2.4^{+0.9}_{-0.3}$	1.49 (81)
27	2022-12-08 04:06:57	1035	>1.7	$11.3^{+10.4}_{-6.1}$	$22.2^{+8.9}_{-10.9}$	$0.05^{+0.04}_{-0.02}$	$2.1^{+0.2}_{-0.1}$	1.35 (93)
28	2022-12-09 12:47:25	458	>1.4	$6.0^{+27.5}_{-5.2}$	<32.7	$0.03^{+0.05}_{-0.02}$	$1.7 \pm 0.2$	1.08 (83)
29	2022-12-13 17:21:58	770	>1.3	$7.1^{+4.9}_{-4.5}$	<27.4	$0.03^{+0.04}_{-0.02}$	$1.6 \pm 0.3$	1.38 (99)
30	2022-12-14 05:45:46	747	$2.0^{+1.2}_{-0.4}$	$13.1^{+10.2}_{-6.5}$	$15.1^{+7.6}_{-9.8}$	$0.05^{+0.05}_{-0.02}$	$1.9^{+0.2}_{-0.1}$	1.28 (79)
31	2022-12-16 08:51:32	3208	$3.1^{+2.6}_{-1.0}$	$7.9^{+4.6}_{-2.4}$	$17.7^{+3.3}_{-5.1}$	$0.04^{+0.03}_{-0.01}$	$1.7 \pm 0.1$	1.17 (99)
32	2022-12-17 06:59:29	3121	$6.3^{+3.6}_{-2.7}$	$7.0^{+2.8}_{-1.1}$	$18.8^{+1.8}_{-3.8}$	$0.04^{+0.02}_{-0.01}$	$1.6 \pm 0.1$	1.24 (97)
33	2022-12-19 01:53:54	7413	$5.4^{+3.0}_{-1.0}$	$42.8^{+4.7}_{-4.1}$	$24.6^{+3.0}_{-3.1}$	$0.06^{+0.02}_{-0.01}$	$5.2 \pm 0.2$	0.96 (118)
34	2022-12-20 01:07:34	800	$3.8^{+1.3}_{-0.6}$	$41.5^{+4.4}_{-6.5}$	$12.8^{+8.1}_{-4.9}$	$0.11^{+0.11}_{-0.04}$	$4.5 \pm 0.2$	1.31 (91)
35	2022-12-21 11:29:21	3371	>5.1	$18.4^{+3.0}_{-1.2}$	$22.1^{+2.2}_{-5.5}$	$0.05^{+0.03}_{-0.01}$	$2.9^{+0.2}_{-0.1}$	1.09 (105)
36	2022-12-22 13:49:16	4153	>4.5	$13.5^{+4.1}_{-1.2}$	$22.9^{+2.8}_{-5.3}$	$0.04^{+0.02}_{-0.01}$	$2.4^{+0.2}_{-0.1}$	1.30 (111)
37	2022-12-23 02:13:06	5002	>5.0	$12.8^{+2.1}_{-1.0}$	$19.7^{+4.1}_{-3.4}$	$0.04^{+0.02}_{-0.01}$	$2.2^{+0.2}_{-0.1}$	1.37 (111)
38	2022-12-24 07:19:35	7342	>3.7	$10.2^{+3.1}_{-2.0}$	$21.8^{+1.6}_{-3.1}$	$0.04 \pm 0.01$	$1.8 \pm 0.1$	1.25 (114)
39	2022-12-25 00:41:18	7515	>3.6	$10.2^{+2.0}_{-1.4}$	$19.7^{+2.4}_{-3.1}$	$0.04^{+0.02}_{-0.01}$	$1.9 \pm 0.1$	1.43 (109)
40	2022-12-26 04:20:27	3148	>1.6	$7.3^{+7.5}_{-3.9}$	$20.2^{+5.1}_{-7.7}$	$0.04^{+0.02}_{-0.01}$	$1.6 \pm 0.1$	1.11 (113)
41	2022-12-27 00:50:45	5203	>2.1	$12.2^{+5.2}_{-3.7}$	$15.1^{+6.7}_{-6.1}$	$0.05^{+0.04}_{-0.02}$	$1.9^{+0.3}_{-0.2}$	1.16 (122)
42	2022-12-28 01:40:40	4243	>2.8	$11.2^{+2.9}_{-3.1}$	$15.0^{+4.4}_{-3.5}$	$0.05^{+0.03}_{-0.01}$	$1.6 \pm 0.1$	1.37 (116)
43	2022-12-29 11:32:56	1172	>1.3	$12.7^{+12.3}_{-9.3}$	<22.7	$0.06^{+0.05}_{-0.02}$	$1.5 \pm 0.1$	1.24 (94)
44	2022-12-30 08:53:17	1251	>1.2	$6.9^{+16.8}_{-6.0}$	<22.3	$0.05^{+0.04}_{-0.02}$	$1.4^{+0.2}_{-0.1}$	1.17 (99)
45	2022-12-31 08:06:36	985	>2.5	$6.4^{+2.1}_{-3.0}$	$19.3^{+2.3}_{-4.2}$	$0.04^{+0.03}_{-0.01}$	$1.3^{+0.3}_{-0.1}$	0.93 (88)
46	2023-01-01 02:41:31	531	>1.3	$4.8^{+21.8}_{-4.5}$	<26.3	<0.02	$1.4^{+0.4}_{-0.2}$	0.96 (81)
47	2023-01-02 01:55:13	1246	>1.6	$8.4^{+7.2}_{-4.8}$	$13.6^{+6.8}_{-6.9}$	$0.07^{+0.05}_{-0.03}$	$1.6 \pm 0.1$	0.94 (91)
48	2023-01-04 15:51:36	935	>2.9	$8.1^{+5.6}_{-2.0}$	$14.4^{+4.1}_{-7.7}$	$0.05^{+0.08}_{-0.02}$	$1.5^{+0.2}_{-0.1}$	1.07 (94)
49	2023-01-06 01:56:07	2534	>3.3	$7.6^{+1.4}_{-2.6}$	$17.9^{+1.6}_{-3.9}$	$0.04^{+0.02}_{-0.01}$	$1.5 \pm 0.1$	0.95 (96)
50	2023-01-07 22:58:22	846	$2.3^{+1.8}_{-0.5}$	$7.6^{+5.6}_{-2.7}$	$11.1^{+3.5}_{-5.9}$	$0.08^{+0.08}_{-0.03}$	$1.3 \pm 0.1$	1.49 (80)
51	2023-01-09 05:50:26	1242	>2.4	$4.3^{+4.3}_{-1.8}$	$17.6^{+2.8}_{-5.0}$	$0.03^{+0.03}_{-0.01}$	$1.2^{+0.1}_{-0.2}$	1.54 (83)
52	2023-01-10 15:55:57	1211	>4.6	$10.2^{+2.1}_{-3.4}$	$21.0^{+1.8}_{-2.9}$	$0.02^{+0.03}_{-0.01}$	$1.6^{+0.2}_{-0.1}$	1.09 (91)
53	2023-01-11 18:16:33	1175	>4.2	$7.4^{+2.3}_{-3.6}$	$20.8^{+1.9}_{-1.4}$	$0.03^{+0.03}_{-0.01}$	$1.4^{+0.2}_{-0.1}$	0.87 (90)
54	2023-01-12 20:36:55	1153	>2.8	$10.0^{+4.3}_{-3.1}$	$12.8^{+4.8}_{-5.3}$	$0.06^{+0.07}_{-0.02}$	$1.6^{+0.1}_{-0.2}$	1.30 (84)

Table A.1 continued

Table A.1 (continued)

No.	Obs. Start time (UTC)	Exposure time (s)	$kT_{\text{hot}}^a$ (keV)	$EM_{\text{hot}}^b$ ( $10^{54} \text{ cm}^{-3}$ )	$EM_{\text{cool}}^b$ ( $10^{54} \text{ cm}^{-3}$ )	$Z^c$ ( $Z_{\odot}$ )	$L_X$ ( $10^{32} \text{ erg s}^{-1}$ )	$\chi^2_{\nu}$ (d.o.f.) <sup>d</sup>
55	2023-01-13 18:18:18	1170	>4.1	$7.6^{+2.0}_{-2.8}$	$21.4^{+2.0}_{-2.7}$	$0.05^{+0.03}_{-0.01}$	$1.7 \pm 0.1$	1.22 (90)
56	2023-01-15 01:17:22	1126	>2.6	$9.4^{+3.6}_{-3.7}$	$19.0^{+3.1}_{-7.5}$	$0.04^{+0.04}_{-0.02}$	$1.6^{+0.3}_{-0.1}$	1.00 (93)
57	2023-01-16 12:54:38	1130	>2.8	$10.2^{+4.2}_{-2.5}$	$21.5^{+3.1}_{-7.0}$	$0.02^{+0.03}_{-0.01}$	$1.9^{+0.2}_{-0.1}$	1.21 (89)
58	2023-01-17 21:25:40	1148	$3.5^{+2.3}_{-1.0}$	$15.5^{+6.6}_{-4.4}$	$14.4^{+6.0}_{-7.5}$	$0.04^{+0.05}_{-0.02}$	$2.1^{+0.2}_{-0.1}$	0.88 (86)
59	2023-01-19 07:29:44	1164	>6.2	$11.9^{+2.7}_{-1.5}$	$21.1^{+2.3}_{-5.2}$	$0.04^{+0.03}_{-0.01}$	$1.9^{+0.2}_{-0.1}$	1.34 (89)
60	2023-01-21 12:19:49	2021	>5.3	$6.5^{+1.5}_{-2.0}$	$18.1^{+1.3}_{-1.9}$	$0.04^{+0.02}_{-0.01}$	$1.4 \pm 0.1$	1.20 (95)
61	2023-01-23 02:50:28	660	<2.2	>19.0	<18.3	<0.03	$1.3 \pm 0.1$	1.17 (97)
62	2023-01-24 17:39:33	915	$2.0^{+6.2}_{-0.5}$	$4.8^{+6.3}_{-3.2}$	$15.6^{+4.2}_{-6.3}$	$0.05^{+0.04}_{-0.02}$	$1.2 \pm 0.1$	1.90 (81)
63	2023-01-25 09:00:24	1424	$1.7^{+0.9}_{-0.3}$	$11.8^{+11.2}_{-7.0}$	<18.1	$0.03^{+0.04}_{-0.02}$	$1.3 \pm 0.1$	1.61 (84)
64	2023-01-26 14:25:23	1018	>3.3	$6.8^{+2.7}_{-3.7}$	$19.5^{+2.8}_{-3.9}$	$0.03^{+0.03}_{-0.02}$	$1.5^{+0.1}_{-0.2}$	1.18 (88)
65	2023-01-27 05:59:15	1329	>4.7	$6.9^{+1.7}_{-2.5}$	$19.1 \pm 2.0$	$0.03^{+0.03}_{-0.01}$	$1.5^{+0.1}_{-0.2}$	1.52 (88)
66	2023-01-29 12:05:21	1593	$2.5^{+5.9}_{-1.1}$	$5.6^{+14.5}_{-3.8}$	<18.9	$0.02^{+0.03}_{-0.01}$	$1.1 \pm 0.1$	1.17 (86)
67	2023-02-02 18:43:04	1214	>1.5	$7.6^{+5.2}_{-4.1}$	$6.4^{+7.0}_{-2.0}$	$0.10^{+0.13}_{-0.06}$	$0.9^{+0.2}_{-0.1}$	1.17 (87)
68	2023-02-06 18:17:07	2287	>2.4	$11.6^{+7.8}_{-4.3}$	$26.2^{+3.8}_{-14.6}$	$0.03^{+0.03}_{-0.01}$	$2.4^{+0.2}_{-0.1}$	1.10 (76)

NOTE—All 68 observations' spectra were fitted by 2T `apec` model in 0.3–10 keV except for the spectra of observation ID 5203530122 and 5203530169, which were both dominated by background at around 10 keV and were fitted only in 0.3–8.0 keV and 0.3–6.0 keV respectively. All errors represent the 90% uncertainties.

<sup>a</sup>Plasma temperature of the hot component.

<sup>b</sup>The EM of the hot and cool components, calculated as  $EM = 4\pi d^2 \times 10^{14} \text{ norm}$ , where  $\text{norm}$  is one of the parameters in `apec` model.

<sup>c</sup>Metal abundance.

<sup>d</sup>Reduced  $\chi^2$  ( $\chi^2_{\nu}$ ) and degrees of freedom (d.o.f.)

## B. DETAILED CALCULATIONS ABOUT FLARING LOOP

If the flare occurred inside closed loop structures, the cooling timescale should increase with the size of the loops. As [Wargelin et al. \(2008\)](#) summarized, when a flare is dominated by conductive losses, its cooling timescale can be expressed as

$$\tau_C = \frac{4 \times 10^{-10} n_e L^2}{T^{5/2}}, \quad (\text{B1})$$

where  $n_e$  is the electron density,  $L$  is the half-length of the flaring loop, and  $T$  is the temperature of the flaring plasma.  $n_e$  is related to  $EM$  by  $EM = n_e n_H V \sim 0.85 n_e^2 V$  for cosmic abundances. When a flare is dominated by radiative losses, the cooling timescale is given by

$$\tau_R = \frac{3kT}{n_e \Lambda(T)}. \quad (\text{B2})$$

Here  $\Lambda(T)$  is the cooling function of flaring plasma, whose specific form is subject to the temperature  $T$ . For  $T \geq 20$  MK,  $\Lambda(T) \approx 10^{-24.66} T^{1/4}$  ([Güdel 2004](#)).

During the fast decay phase of MF, due to the lack of constraints on  $T_{\text{hot}}$  from *LEIA* data, we could only infer that the temperature near the flare peak is at least as high as the maximum  $T_{\text{hot}}$  obtained by *NICER* data. At such

**Table A.2.** Best-fit Spectral parameters for each *LEIA* observation

No.	Obs. Start time (UTC)	Exposure time (s)	$kT_{\text{hot}}$ keV	$EM_{\text{hot}}$ $10^{54} \text{ cm}^{-3}$	$EM_{\text{cool}}$ $10^{54} \text{ cm}^{-3}$	$L_X$ $10^{32} \text{ erg s}^{-1}$	$\chi^2_{\nu}$ (d.o.f.)
01	2022-11-07 06:26:36	1110	...	<301	<261	$19^{+9.4}_{-12.9}$	1.25 (35)
02	2022-11-07 09:35:57	1097	>1.8	$345^{+116}_{-207}$	<231	$31.1^{+13.8}_{-7.3}$	0.82 (35)
03	2022-11-07 11:10:37	1110	>2.9	$339^{+89}_{-136}$	<123	$34.8^{+20.6}_{-12.0}$	0.98 (42)
04	2022-11-07 19:04:00	2087*	>5.1	$777^{+105}_{-217}$	<206	$84.5^{+9.9}_{-17.2}$	1.04 (19)
05	2022-11-08 09:16:03	2180*	>2.6	$1051^{+157}_{-204}$	<222	$94.9^{+19.7}_{-17.3}$	0.97 (24)
06	2022-11-08 15:34:44	3240*	>3.3	$521^{+213}_{-213}$	<477	$70.9^{+10.3}_{-13.4}$	0.96 (29)
07	2022-11-09 08:56:08	3240*	>4.0	$463^{+90}_{-167}$	<196	$49.3^{+10.2}_{-9.7}$	1.46 (26)
08	2022-11-09 15:14:49	2828*	>1.8	$267^{+147}_{-142}$	<312	$34.5^{+7.8}_{-7.0}$	0.58 (21)
09	2022-11-10 10:10:53	2178*	>2.0	$311^{+67}_{-152}$	<163	$30.6^{+8.9}_{-8.2}$	0.99 (13)
10	2022-11-10 14:54:53	3161*	>2.0	$281^{+44}_{-87}$	<52	$24.6^{+7.8}_{-5.5}$	1.15 (17)
11	2022-11-11 08:16:16	4186*	...	<181	<253	$17.9^{+6.8}_{-5.5}$	0.58 (19)
12	2022-11-12 11:04:04	5491*	>1.7	$146^{+34}_{-86}$	<99	$14.3 \pm 4.4$	0.85 (18)
13	2022-11-13 09:09:23	3263*	...	<158	<134	$14.8^{+5.2}_{-9.8}$	1.04 (8)
14	2022-11-14 16:42:59	1073	...	<229	<222	$8.3^{+23.2}_{-3.2}$	1.13 (26)
15	2022-11-16 12:52:49	2202*	...	<178	<149	$12.4^{+4.8}_{-6.4}$	1.19 (4)
16	2022-11-17 12:32:31	1104	...	<171	<146	$5.7^{+7.0}_{-2.0}$	1.51 (24)
17	2022-11-18 09:02:56	2166*	>1.5	$132^{+50}_{-89}$	<99	$12.9^{+21.3}_{-5.9}$	1.58 (4)

\*Data from consecutive observations are combined for better spectral analysis.

**Table A.3.** Best-fit Spectral parameters for each *Swift*/XRT observation

No.	Obs. Start time (UTC)	Exposure time (s)	$kT_{\text{hot}}$ (keV)	$EM_{\text{hot}}$ ( $10^{54} \text{ cm}^{-3}$ )	$EM_{\text{cool}}$ ( $10^{54} \text{ cm}^{-3}$ )	$Z$ ( $Z_{\odot}$ )	$L_X$ ( $10^{32} \text{ erg s}^{-1}$ )	$\chi^2_{\nu}$ (d.o.f.)
01	2022-11-09 15:11:58	1493	$6.0^{+2.6}_{-1.2}$	$373.1^{+52.8}_{-38.9}$	<55.1	>0.02	$42.8^{+5.5}_{-3.3}$	0.81 (130)
02	2022-11-15 06:30:02	539	$2.8^{+2.7}_{-0.6}$	$104.1^{+26.9}_{-50.9}$	<66.7	<0.18	$8.8^{+1.1}_{-1.0}$	1.08 (59)
03	2022-11-16 14:20:08	1432	>2.4	$50.4^{+19.0}_{-13.4}$	$55.9 \pm 27.0$	$0.06^{+0.08}_{-0.04}$	$8.0^{+1.1}_{-0.9}$	0.92 (108)
04	2022-11-17 09:16:47	973	>4.7	$36.8^{+11.1}_{-7.4}$	$60.6^{+13.4}_{-21.2}$	<0.06	$6.2 \pm 0.4$	1.30 (79)
05	2022-12-25 05:13:10	1478	>6.7	$9.9^{+7.4}_{-3.1}$	$14.9^{+5.5}_{-11.0}$	<0.15	$1.8^{+0.3}_{-0.5}$	1.26 (24)

a high temperature, conductive losses are likely the dominant factor. Therefore we set  $\tau_C$  in Equation (B1) to be  $\tau_{\text{d,MF1}} = 109$  ks. Assuming the flaring plasma is confined in a single loop with constant cross section, the volume of the loop is given by

$$V = 2\pi\beta^2 L^3, \quad (\text{B3})$$

where  $\beta = r/L$  is the loop aspect ratio, and  $r$  is the radius of the loop cross section. In addition, the maximum temperature  $T_{\text{max}}$  inside the loop structure, electron density  $n_e$ , and the loop half-length  $L$  obey the RTV scaling law (Rosner et al. 1978),

$$T_{\text{max}}^2 \approx 7.6 \times 10^{-7} n_e L, \quad (\text{B4})$$

**Table A.4.** Results of Balmer Lines Measurements from First Lijiang 2.4m Telescope Observation.

	Flux <sup>a</sup>	FWHM <sup>b</sup>	$\Delta V$ <sup>c</sup>	$V_{\max}$ <sup>d</sup>
	( $10^{-12}$ erg cm <sup>-2</sup> s <sup>-1</sup> )	(km s <sup>-1</sup> )	(km s <sup>-1</sup> )	(km s <sup>-1</sup> )
H $\alpha$	39.0 $\pm$ 0.4	169 $\pm$ 1	33.1 $\pm$ 0.6	180
H $\beta$	6.3 $\pm$ 0.1	101 $\pm$ 1	14.3 $\pm$ 0.5	105
H $\gamma$	3.7 $\pm$ 0.1	122 $\pm$ 2	11.7 $\pm$ 0.9	111
H $\delta$	3.1 $\pm$ 0.1	164 $\pm$ 4	12.8 $\pm$ 1.6	125

<sup>a</sup>The measured line flux.

<sup>b</sup>The measured line width after a correction of instrumental profile.

<sup>c</sup>The projected velocity of line center.

<sup>d</sup>The maximum projected velocity as the wavelength where the residual profile lies  $1\sigma$  above the continuum. The instrumental profile is corrected.

under the hypothesis of a loop in hydrostatic equilibrium with uniform heating. Using Equation (B1) and the RTV scaling law, the loop size  $L$  and electron density  $n_e$  can be both derived, as well as  $V$  and  $\beta$ . Furthermore, the pressure  $p$  inside the loop and the minimum magnetic field  $B$  of the flaring plasma can be estimated by

$$p = 2n_e kT, \quad (\text{B5})$$

and

$$B = \sqrt{8\pi p}. \quad (\text{B6})$$

We remind that the loop size may be underestimated because the actual peak  $kT_{\text{hot}}$  can be much higher than 6.8 keV. For comparison, these parameters are also derived using *LEIA* data assuming the peak  $kT_{\text{hot}}$  of 10 keV and 20 keV. The results of the parameters are listed in Table B.1. Note that  $T_{\text{max}}$  is distinct from the maximum best-fit temperature  $T_{\text{obs}}$ , which is the average loop temperature. For simplicity, this difference is neglected in our calculations; however, we again emphasize that  $T_{\text{obs}}$  could be much higher than the 79 MK observed and  $T_{\text{max}}$  is somewhat higher than  $T_{\text{obs}}$ .

To apply the RTV scaling law, a constant pressure throughout the whole loop is required, which means the size of loop  $L$  should be smaller than the the pressure scale height of the stellar atmosphere with  $H = kT/\mu m_p g$ , where  $\mu$  is the average mass coefficient of plasma particle ( $\sim 1/2$  in a fully ionized plasma),  $m_p$  is the proton mass and  $g$  is the gravitational acceleration at the stellar surface. So we derived  $H \sim 1 \times 10^{14}$  cm, which is much larger than the  $L \sim 1.8 \times 10^{12}$  cm estimated above, confirming the applicability of the RTV scaling law here.

During the cooling stage of the flaring plasma, the radiative loss gradually dominate the slow decay phase. In this phase, the initial heat pulse subsided, while a post-flare arcade built up. If we took the assumption that the loops inside the arcade all reached the same peak temperature simultaneously and had similar cooling processes, the arcade can be regarded as a single loop obeying the same cooling function  $\Lambda(T)$ . Then using Equation (B2),  $\tau_R = \tau_{\text{d,MF2}} = 869$  ks,  $T_{\text{hot}} \approx 60$  MK ( $kT_{\text{hot}} = 5.2$  keV, from the first *NICER* observation after  $t_{\text{p,MF2}}$ , observation ID=5203530104), the electron density can be derived. Provided that the plasma is confined in a hemisphere with a radius  $l = 2L/\pi$ , the volume can be expressed by

$$V = \frac{32}{3\pi^2} L^3. \quad (\text{B7})$$

The derived parameters are displayed in Table B.1 as well.

In addition, the loop size can also be constrained by the rise timescale of the flare. During the rise phase, the high energy electrons generated by magnetic reconnection zoomed along the loops, and bombarded the footpoints continuously, violently heating the chromospheric material, which evaporated to fill the loop afterward and produced



**Table B.1.** Parameters of loop size and flaring plasma.

	$L^a$	$n_e^b$	$V^c$	$\beta^d$	$p^e$	$B^f$
	( $10^{12}$ cm)	( $10^9$ cm $^{-3}$ )	$10^{36}$ cm $^3$		dyne cm $^{-2}$	(gauss)
MF1*	$1.8 \pm 0.2$	$4.5^{+0.9}_{-1.0}$	$18.9^{+7.6}_{-8.7}$	$0.69^{+0.17}_{-0.19}$	$97.2^{+21.2}_{-24.3}$	$49.4^{+5.4}_{-6.2}$
MF1 $\dagger$	2.2	8.0	19.5	0.53	255	80.0
MF1 $\ddagger$	3.2	22.5	2.4	0.11	1442	190
MF2*	$4.1^{+0.3}_{-0.2}$	$1.5^{+0.2}_{-0.1}$	$72.1^{+16.2}_{-12.1}$	...	$24.8^{+4.3}_{-3.1}$	$25.0^{+2.2}_{-1.6}$
SF*	$1.0^{+0.3}_{-0.1}$	$6.5^{+2.8}_{-1.2}$	$1.2^{+1.0}_{-0.5}$	...	$112.2^{+79.0}_{-29.1}$	$53.1^{+18.7}_{-6.9}$

NOTE—Since the light curve of SF does not deviate from a single exponential decay, the conductive cooling phase is assumed to be skipped (Reale 2007). The cooling process of SF is then solely dominated by radiative loss.

\*Estimations based on *NICER* data.

$\dagger$  Estimations based on *LEIA* data,  $kT_{\text{hot,peak}} = 10$  keV is assumed.

$\ddagger$  Estimations based on *LEIA* data,  $kT_{\text{hot,peak}} = 20$  keV is assumed.

<sup>a</sup>Half-length of flaring loop(s).

<sup>b</sup>Electron density.

<sup>c</sup>The volume of flaring plasma.

<sup>d</sup>Loop aspect ratio.

<sup>e</sup>Pressure inside the flaring loop(s).

<sup>f</sup>The magnetic field strength required to confine the flaring plasma.

soft X-ray radiation. It is well-known that the timescale of this filling process should not exceed  $L/c_s$ . Here the sound speed of the plasma is  $c_s = \sqrt{kT/\mu m_p}$ . Using the rise timescale of the MF  $\tau_{\text{r, MF1}} = 112$  ks, an upper limit of the half-length of the initial single loop is suggested to be  $\sim 1.3 \times 10^{13}$  cm.

Note that the cooling process described here differs from the quasi-static cooling process (van den Oord & Mewe 1989), which requires a constant ratio between the radiative and conductive cooling timescales and the relevant flaring parameters (either  $kT_{\text{hot}}$  or  $EM_{\text{hot}}$ ) decaying exponentially. It also differs from the cooling process with sustained heating proposed by Reale et al. (1997), which may represent a more universal feature of stellar flares. We plan to explore these models further in our future work.

### C. ASAS-SN LONG-TERM LIGHT CURVE

The photometric data from ASAS-SN Sky Patrol v1.0 are used to examine the magnetic activity of HD 251108. The light curve was divided into 22 epochs (7 epochs for the *V*-band and 15 epochs for the *g*-band), and each light curve was folded using a 42.53-day period, which was derived from a periodicity analysis. The normalized light curves for all 22 epochs are shown in Figure C1. The red lines represent the sinusoidal fit for the first folded light curve from 2014. The significant variation in amplitude across the epochs reveals the long-term evolution of large star spots in active regions on the stellar surface.

Analogous to solar cycles, the long-term ASAS-SN light curve spanning from 2014 to 2024 clearly indicates a stellar cycle lasting over 10 years (Figure C2). We further defined a flux variation ratio  $\Delta F/\bar{F}$  as follows,

$$\Delta F/\bar{F} = \frac{F_{95\%} - F_{5\%}}{\bar{F}}, \quad (\text{C1})$$

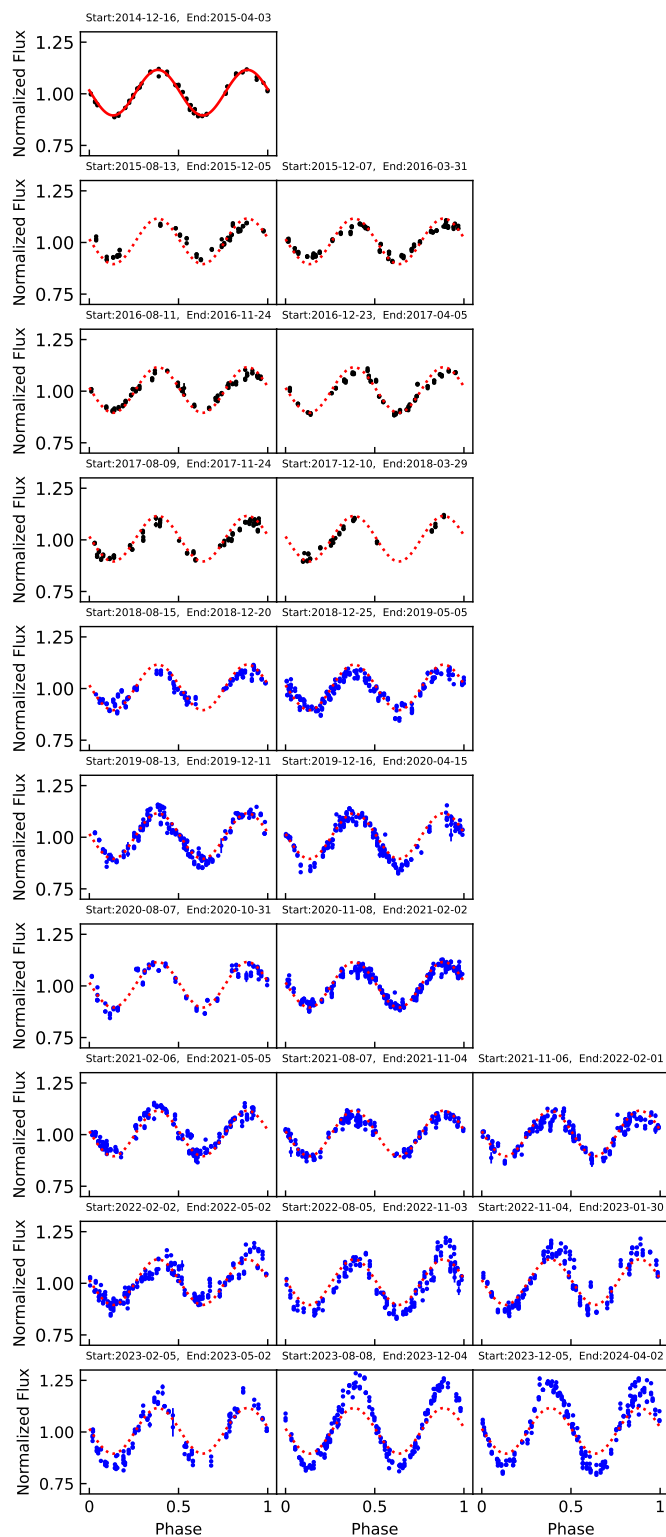


**Figure C1.** The normalized light curves from ASAS-SN V-band (black points) and *g*-band (blue points). The red line (solid or dotted) in each panel is the sinusoidal fitting result of light curve from the first group.

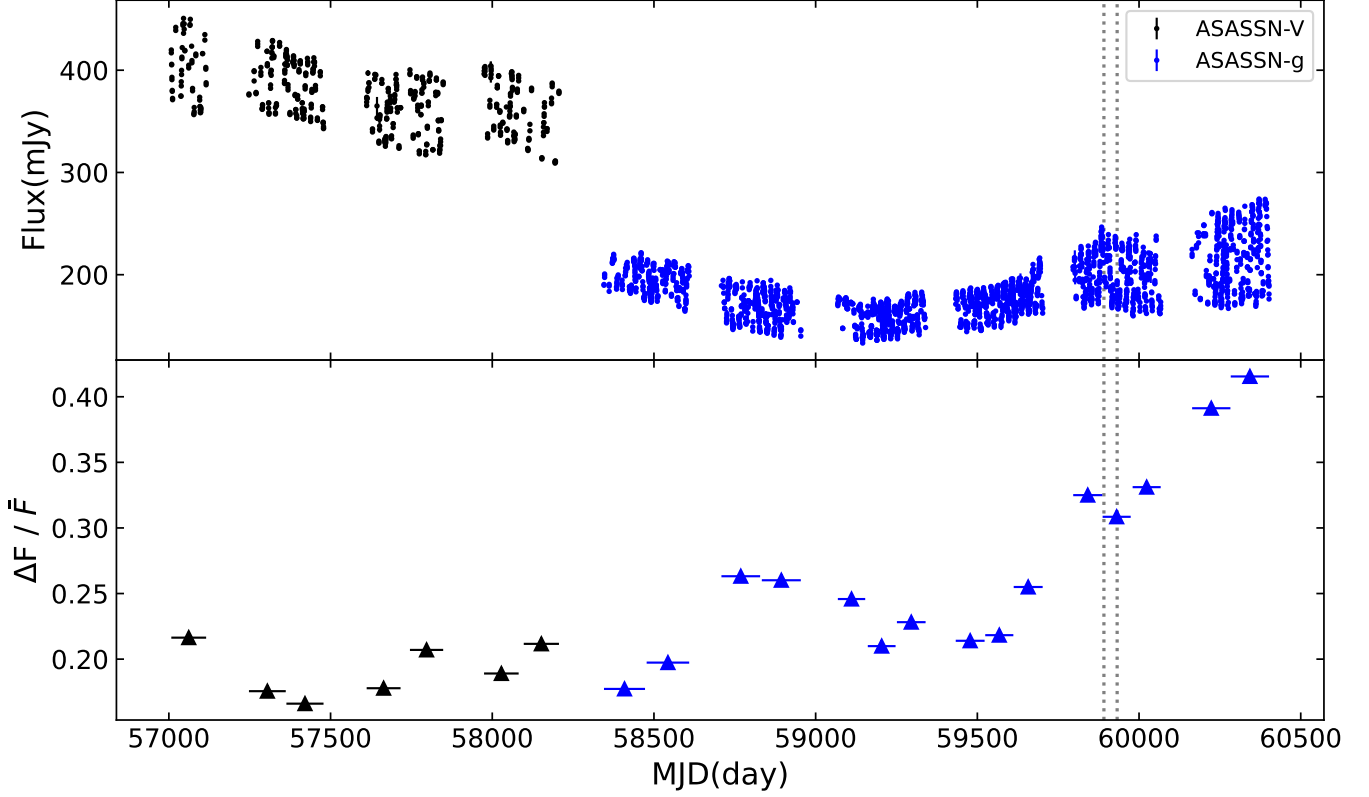


**Figure C2.** The entire light curves from ASAS-SN  $V$ -band and  $g$ -band (top panel) and the temporal evolution of  $\Delta F/\bar{F}$  (bottom panel). The gray dotted lines mark the time MF and SF occur.

where  $\bar{F}$  is the mean value of flux and  $F_{95\%}$  and  $F_{5\%}$  are the 95th and 5th percentile flux, respectively. The variation ratio  $\Delta F/\bar{F}$  was calculated for each epoch in Figure C1, and its temporal variation further confirms the presence of a stellar cycle lasting over a decade.

We then used PHOEBE (Prša et al. 2016; Horvat et al. 2018; Conroy et al. 2020) to simultaneously fit the multi-year light curves of the system by including two cool spots on the visible star. Given the quality of the light curves and the time cost for fitting, we focused on the  $g$ -band light curves from 2018 to 2021, specifically the second one from 2018, the first from 2019, the second from 2020, and the third from 2021. During the modeling process, the period and eccentricity were fixed at  $P = 42.53$  day and  $e = 0$ , respectively, while a linear correlation between mass and radius was assumed for the companion main-sequence star.

From the fitting, we derived the inclination angle of the binary orbit to be  $68.63^{+1.73}_{-1.25}^\circ$  and the mass ratio to be  $q = 0.33^{+0.03}_{-0.03}$ . Simultaneously, we obtained  $M_{\text{giant}} = 0.26^{+0.04}_{-0.01} M_\odot$ ,  $R_{\text{giant}} = 13.69^{+0.19}_{-0.21} R_\odot$ , and  $T_{\text{eff,giant}} = 4951^{+40}_{-16}$  K for the giant, and  $T_{\text{eff,com}} = 5400^{+31}_{-68}$  K for the companion. This implies the companion is a G-/K-type main sequence star with a mass of  $M_{\text{com}} = 0.79^{+0.14}_{-0.14} M_\odot$ . Given the accuracy limitations of both methods, the difference between  $T_{\text{eff,giant}}$  from our fitting and that reported by Anders et al. (2019) is acceptable. The binary separation, estimated to around  $50 R_\odot$  from the fitting, suggests that the magnetic loops are unlikely to extend to the companion.

The small mass of the giant indicates it has experienced significant mass loss and is likely a stripped star. Its current mass ( $0.26^{+0.04}_{-0.01} M_\odot$ ) is in good agreement with the orbital period-white dwarf mass relation (Rappaport et al. 1995). Meanwhile, for a tidally locked system, the rotational period of a Roche filling star can be estimated as follows (Wade & Horne 1988),

$$P_{\text{rot}} = \frac{2\pi R_2 \sin i}{0.462 K_2 q^{1/3} (1+q)^{2/3}}, \quad (\text{C2})$$

where the  $R_2$  and the  $K_2$  represent the radius and radial velocity semi-amplitude of the Roche filling star, respectively.  $q = M_2/M_1$  is the mass ratio, and  $i$  is the system inclination. Using the fitting results, the Roche lobe filling factor of HD 251108 can be calculated as about 91.4%, meaning the giant star can be assumed as Roche lobe filling. This leads

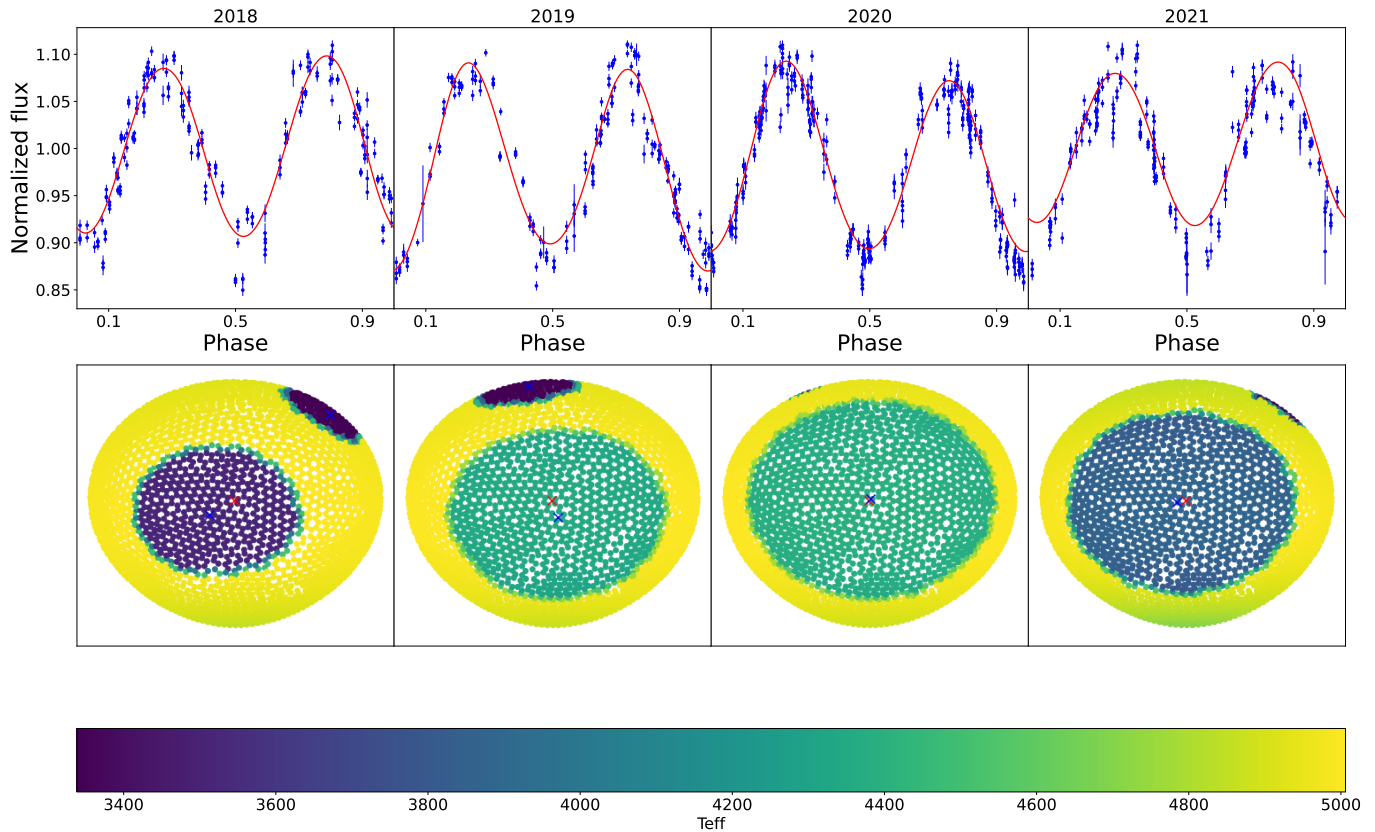


**Figure C3.** Top panel: PHOEBE fitting to the normalized light curves in the ASAS-SN  $g$ -band from 2018 to 2021. Bottom panel: Size and configurations of spots from PHOEBE fitting. The red cross marks the center of the pole, and the blue crosses show the centers of spots.

to a rotational period for the giant of  $40.28^{+0.77}_{-0.78}$  day, consistent with the measured orbital period of HD 251108. All these suggest that the system has experienced mass transfer from the giant star to the main-sequence star through Roche lobe overflow.

## REFERENCES

- Anders, F., Khalatyan, A., Chiappini, C., et al. 2019, *A&A*, 628, A94, doi: [10.1051/0004-6361/201935765](https://doi.org/10.1051/0004-6361/201935765)
- Arnaud, K. A. 1996, in *Astronomical Society of the Pacific Conference Series*, Vol. 101, *Astronomical Data Analysis Software and Systems V*, ed. G. H. Jacoby & J. Barnes, 17
- Aschwanden, M. J., & Alexander, D. 2001, *SoPh*, 204, 91, doi: [10.1023/A:1014257826116](https://doi.org/10.1023/A:1014257826116)
- Bailer-Jones, C. A. L., Rybizki, J., Fouesneau, M., Demleitner, M., & Andrae, R. 2021, *AJ*, 161, 147, doi: [10.3847/1538-3881/abd806](https://doi.org/10.3847/1538-3881/abd806)
- Benz, A. 2002, *Plasma Astrophysics*, second edition, Vol. 279, doi: [10.1007/0-306-47719-X](https://doi.org/10.1007/0-306-47719-X)
- Benz, A. O., & Güdel, M. 2010, *ARA&A*, 48, 241, doi: [10.1146/annurev-astro-082708-101757](https://doi.org/10.1146/annurev-astro-082708-101757)
- Boller, T., Freyberg, M. J., Trümper, J., et al. 2016, *A&A*, 588, A103, doi: [10.1051/0004-6361/201525648](https://doi.org/10.1051/0004-6361/201525648)
- Candelaresi, S., Hillier, A., Maehara, H., Brandenburg, A., & Shibata, K. 2014, *ApJ*, 792, 67, doi: [10.1088/0004-637X/792/1/67](https://doi.org/10.1088/0004-637X/792/1/67)
- Cheng, H., Ling, Z., Zhang, C., et al. 2024, *Experimental Astronomy*, 57, 10, doi: [10.1007/s10686-024-09932-0](https://doi.org/10.1007/s10686-024-09932-0)
- Conroy, K. E., Kochoska, A., Hey, D., et al. 2020, *ApJS*, 250, 34, doi: [10.3847/1538-4365/abb4e2](https://doi.org/10.3847/1538-4365/abb4e2)
- Davenport, J. R. A. 2016, *ApJ*, 829, 23, doi: [10.3847/0004-637X/829/1/23](https://doi.org/10.3847/0004-637X/829/1/23)
- Drake, A. J. 2006, *AJ*, 131, 1044, doi: [10.1086/499102](https://doi.org/10.1086/499102)
- Drake, A. J., Graham, M. J., Djorgovski, S. G., et al. 2014, *ApJS*, 213, 9, doi: [10.1088/0067-0049/213/1/9](https://doi.org/10.1088/0067-0049/213/1/9)
- Emslie, A. G., Dennis, B. R., Shih, A. Y., et al. 2012, *ApJ*, 759, 71, doi: [10.1088/0004-637X/759/1/71](https://doi.org/10.1088/0004-637X/759/1/71)

- Endl, M., Strassmeier, K. G., & Kurster, M. 1997, *A&A*, 328, 565
- Favata, F., & Schmitt, J. H. M. M. 1999, *A&A*, 350, 900, doi: [10.48550/arXiv.astro-ph/9909041](https://doi.org/10.48550/arXiv.astro-ph/9909041)
- Feldman, U., Laming, J. M., & Doschek, G. A. 1995, *ApJL*, 451, L79, doi: [10.1086/309695](https://doi.org/10.1086/309695)
- Franciosini, E., Pallavicini, R., & Tagliaferri, G. 2001, *A&A*, 375, 196, doi: [10.1051/0004-6361:20010830](https://doi.org/10.1051/0004-6361:20010830)
- Getman, K. V., & Feigelson, E. D. 2021, *ApJ*, 916, 32, doi: [10.3847/1538-4357/ac00be](https://doi.org/10.3847/1538-4357/ac00be)
- Getman, K. V., Feigelson, E. D., Broos, P. S., Micela, G., & Garmire, G. P. 2008, *ApJ*, 688, 418, doi: [10.1086/592033](https://doi.org/10.1086/592033)
- Getman, K. V., Feigelson, E. D., & Garmire, G. P. 2021, *ApJ*, 920, 154, doi: [10.3847/1538-4357/ac1746](https://doi.org/10.3847/1538-4357/ac1746)
- Güdel, M. 2004, *A&A Rv*, 12, 71, doi: [10.1007/s00159-004-0023-2](https://doi.org/10.1007/s00159-004-0023-2)
- Günther, M. N., Zhan, Z., Seager, S., et al. 2020, *AJ*, 159, 60, doi: [10.3847/1538-3881/ab5d3a](https://doi.org/10.3847/1538-3881/ab5d3a)
- Hawley, S. L., Davenport, J. R. A., Kowalski, A. F., et al. 2014, *ApJ*, 797, 121, doi: [10.1088/0004-637X/797/2/121](https://doi.org/10.1088/0004-637X/797/2/121)
- Horvat, M., Conroy, K. E., Pablo, H., et al. 2018, *ApJS*, 237, 26, doi: [10.3847/1538-4365/aacd0f](https://doi.org/10.3847/1538-4365/aacd0f)
- Karmakar, S., Naik, S., Pandey, J. C., & Savanov, I. S. 2023, *MNRAS*, 518, 900, doi: [10.1093/mnras/stac2970](https://doi.org/10.1093/mnras/stac2970)
- Kashapova, L. K., Broomhall, A.-M., Larionova, A. I., Kupriyanova, E. G., & Motyk, I. D. 2021, *MNRAS*, 502, 3922, doi: [10.1093/mnras/stab276](https://doi.org/10.1093/mnras/stab276)
- Li, D. Y., Ling, Z. X., Liu, Y., et al. 2022, *The Astronomer's Telegram*, 15754, 1
- Lin, J. 2002, *ChJA&A*, 2, 539, doi: [10.1088/1009-9271/2/6/539](https://doi.org/10.1088/1009-9271/2/6/539)
- Lin, J., & Forbes, T. G. 2000, *J. Geophys. Res.*, 105, 2375, doi: [10.1029/1999JA900477](https://doi.org/10.1029/1999JA900477)
- Ling, Z. X., Liu, Y., Zhang, C., et al. 2022, *The Astronomer's Telegram*, 15748, 1
- Ling, Z. X., Sun, X. J., Zhang, C., et al. 2023, *Research in Astronomy and Astrophysics*, 23, 095007, doi: [10.1088/1674-4527/acd593](https://doi.org/10.1088/1674-4527/acd593)
- Lyke, B. W., Higley, A. N., McLane, J. N., et al. 2020, *ApJS*, 250, 8, doi: [10.3847/1538-4365/aba623](https://doi.org/10.3847/1538-4365/aba623)
- Maehara, H., Shibayama, T., Notsu, S., et al. 2012, *Nature*, 485, 478, doi: [10.1038/nature11063](https://doi.org/10.1038/nature11063)
- Martínez, C. I., Mauas, P. J. D., & Buccino, A. P. 2022, *MNRAS*, 512, 4835, doi: [10.1093/mnras/stac755](https://doi.org/10.1093/mnras/stac755)
- Merloni, A., Lamer, G., Liu, T., et al. 2024, *A&A*, 682, A34, doi: [10.1051/0004-6361/202347165](https://doi.org/10.1051/0004-6361/202347165)
- Notsu, Y., Maehara, H., Honda, S., et al. 2019, in *American Astronomical Society Meeting Abstracts*, Vol. 234, *American Astronomical Society Meeting Abstracts #234*, 122.02
- Okamoto, S., Notsu, Y., Maehara, H., et al. 2021, in *The 20.5th Cambridge Workshop on Cool Stars, Stellar Systems, and the Sun (CS20.5)*, *Cambridge Workshop on Cool Stars, Stellar Systems, and the Sun*, 112, doi: [10.5281/zenodo.4563244](https://doi.org/10.5281/zenodo.4563244)
- Osten, R. A., Godet, O., Drake, S., et al. 2010, *ApJ*, 721, 785, doi: [10.1088/0004-637X/721/1/785](https://doi.org/10.1088/0004-637X/721/1/785)
- Osten, R. A., Kowalski, A., Drake, S. A., et al. 2016, *ApJ*, 832, 174, doi: [10.3847/0004-637X/832/2/174](https://doi.org/10.3847/0004-637X/832/2/174)
- Pallavicini, R., Golub, L., Rosner, R., et al. 1981, *ApJ*, 248, 279, doi: [10.1086/159152](https://doi.org/10.1086/159152)
- Pandey, J. C., & Singh, K. P. 2012, *MNRAS*, 419, 1219, doi: [10.1111/j.1365-2966.2011.19776.x](https://doi.org/10.1111/j.1365-2966.2011.19776.x)
- Pasham, D., Hamaguchi, K., Miller, J. M., et al. 2022, *The Astronomer's Telegram*, 15755, 1
- Predehl, P., Andritschke, R., Arefiev, V., et al. 2021, *A&A*, 647, A1, doi: [10.1051/0004-6361/202039313](https://doi.org/10.1051/0004-6361/202039313)
- Prša, A., Conroy, K. E., Horvat, M., et al. 2016, *ApJS*, 227, 29, doi: [10.3847/1538-4365/227/2/29](https://doi.org/10.3847/1538-4365/227/2/29)
- Pye, J. P., Rosen, S., Fyfe, D., & Schröder, A. C. 2015, *A&A*, 581, A28, doi: [10.1051/0004-6361/201526217](https://doi.org/10.1051/0004-6361/201526217)
- Rappaport, S., Podsiadlowski, P., Joss, P. C., Di Stefano, R., & Han, Z. 1995, *MNRAS*, 273, 731, doi: [10.1093/mnras/273.3.731](https://doi.org/10.1093/mnras/273.3.731)
- Reale, F. 2007, *A&A*, 471, 271, doi: [10.1051/0004-6361:20077223](https://doi.org/10.1051/0004-6361:20077223)
- Reale, F., Betta, R., Peres, G., Serio, S., & McTiernan, J. 1997, *A&A*, 325, 782
- Reale, F., Güdel, M., Peres, G., & Audard, M. 2004, *A&A*, 416, 733, doi: [10.1051/0004-6361:20034027](https://doi.org/10.1051/0004-6361:20034027)
- Rosner, R., Tucker, W. H., & Vaiana, G. S. 1978, *ApJ*, 220, 643, doi: [10.1086/155949](https://doi.org/10.1086/155949)
- Sasaki, R., Tsuboi, Y., Iwakiri, W., et al. 2021, *ApJ*, 910, 25, doi: [10.3847/1538-4357/abde38](https://doi.org/10.3847/1538-4357/abde38)
- Shibata, K., & Magara, T. 2011, *Living Reviews in Solar Physics*, 8, 6, doi: [10.12942/lrsp-2011-6](https://doi.org/10.12942/lrsp-2011-6)
- Shibata, K., & Yokoyama, T. 1999, *ApJL*, 526, L49, doi: [10.1086/312354](https://doi.org/10.1086/312354)
- Shibayama, T., Maehara, H., Notsu, S., et al. 2013, *ApJS*, 209, 5, doi: [10.1088/0067-0049/209/1/5](https://doi.org/10.1088/0067-0049/209/1/5)
- Shimizu, T. 1995, *PASJ*, 47, 251
- Smith, R. K., Brickhouse, N. S., Liedahl, D. A., & Raymond, J. C. 2001, *ApJL*, 556, L91, doi: [10.1086/322992](https://doi.org/10.1086/322992)
- Tody, D. 1986, in *Society of Photo-Optical Instrumentation Engineers (SPIE) Conference Series*, Vol. 627, *Instrumentation in astronomy VI*, ed. D. L. Crawford, 733, doi: [10.1117/12.968154](https://doi.org/10.1117/12.968154)

- Tody, D. 1993, in *Astronomical Society of the Pacific Conference Series*, Vol. 52, *Astronomical Data Analysis Software and Systems II*, ed. R. J. Hanisch, R. J. V. Brissenden, & J. Barnes, 173
- Tsuboi, Y., Yamazaki, K., Sugawara, Y., et al. 2016, *PASJ*, 68, 90, doi: [10.1093/pasj/psw081](https://doi.org/10.1093/pasj/psw081)
- Tsuru, T., Makishima, K., Ohashi, T., et al. 1989, *PASJ*, 41, 679
- van den Oord, G. H. J., & Mewe, R. 1989, *A&A*, 213, 245
- Wade, R. A., & Horne, K. 1988, *ApJ*, 324, 411, doi: [10.1086/165905](https://doi.org/10.1086/165905)
- Walkowicz, L. M., Basri, G., Batalha, N., et al. 2011, *AJ*, 141, 50, doi: [10.1088/0004-6256/141/2/50](https://doi.org/10.1088/0004-6256/141/2/50)
- Wang, C.-J., Bai, J.-M., Fan, Y.-F., et al. 2019, *Research in Astronomy and Astrophysics*, 19, 149, doi: [10.1088/1674-4527/19/10/149](https://doi.org/10.1088/1674-4527/19/10/149)
- Wang, J., Xin, L. P., Li, H. L., et al. 2021, *ApJ*, 916, 92, doi: [10.3847/1538-4357/ac096f](https://doi.org/10.3847/1538-4357/ac096f)
- Wargelin, B. J., Kashyap, V. L., Drake, J. J., García-Alvarez, D., & Ratzlaff, P. W. 2008, *ApJ*, 676, 610, doi: [10.1086/528702](https://doi.org/10.1086/528702)
- Wei, J., Cordier, B., Antier, S., et al. 2016, arXiv e-prints, arXiv:1610.06892, doi: [10.48550/arXiv.1610.06892](https://doi.org/10.48550/arXiv.1610.06892)
- Wright, N. J., Drake, J. J., Mamajek, E. E., & Henry, G. W. 2011, *ApJ*, 743, 48, doi: [10.1088/0004-637X/743/1/48](https://doi.org/10.1088/0004-637X/743/1/48)
- Xin, L.-P., Li, H.-l., Wang, J., et al. 2024, *MNRAS*, 527, 2232, doi: [10.1093/mnras/stad960](https://doi.org/10.1093/mnras/stad960)
- Xiong, D. R., Bai, J. M., Fan, Y. F., et al. 2022, *The Astronomer's Telegram*, 15775, 1
- Yuan, W., Zhang, C., Chen, Y., & Ling, Z. 2022, in *Handbook of X-ray and Gamma-ray Astrophysics*, 86, doi: [10.1007/978-981-16-4544-0\\_151-1](https://doi.org/10.1007/978-981-16-4544-0_151-1)
- Zhang, C., Ling, Z. X., Sun, X. J., et al. 2022, *ApJL*, 941, L2, doi: [10.3847/2041-8213/aca32f](https://doi.org/10.3847/2041-8213/aca32f)
- Zhao, X., Wang, S., Li, X., et al. 2024, *ApJ*, 963, 160, doi: [10.3847/1538-4357/ad1e64](https://doi.org/10.3847/1538-4357/ad1e64)